Radiometer Searches for the Persistent Sources of Gravitational Waves using Ground-based Detectors

Deepali Agarwal

Postdoctoral Fellow
CP3, UCLouvain

BelGrav Weekly Meeting

Feb 21, 2024

Gravitational Wave Sources

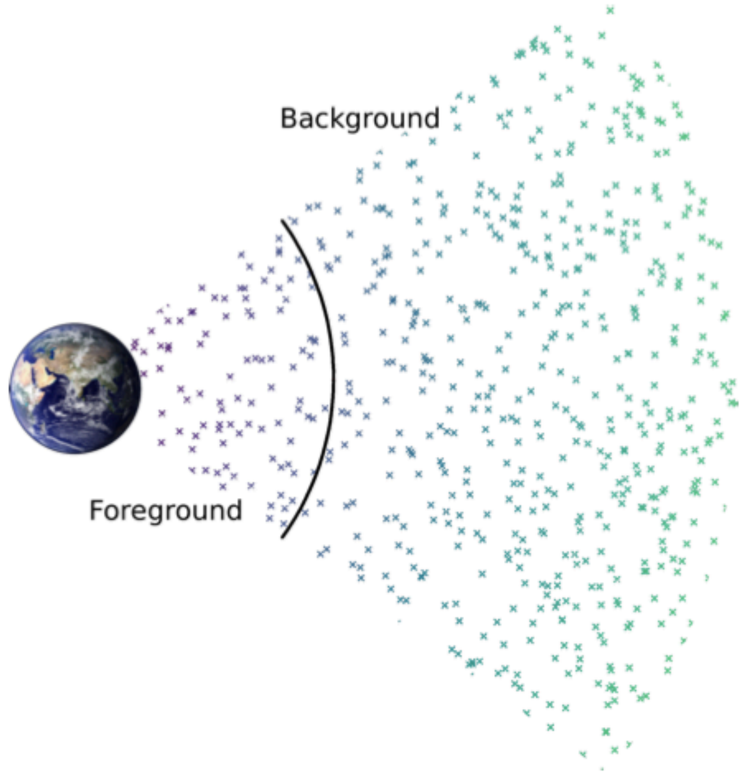

Alexander C. Jenkins

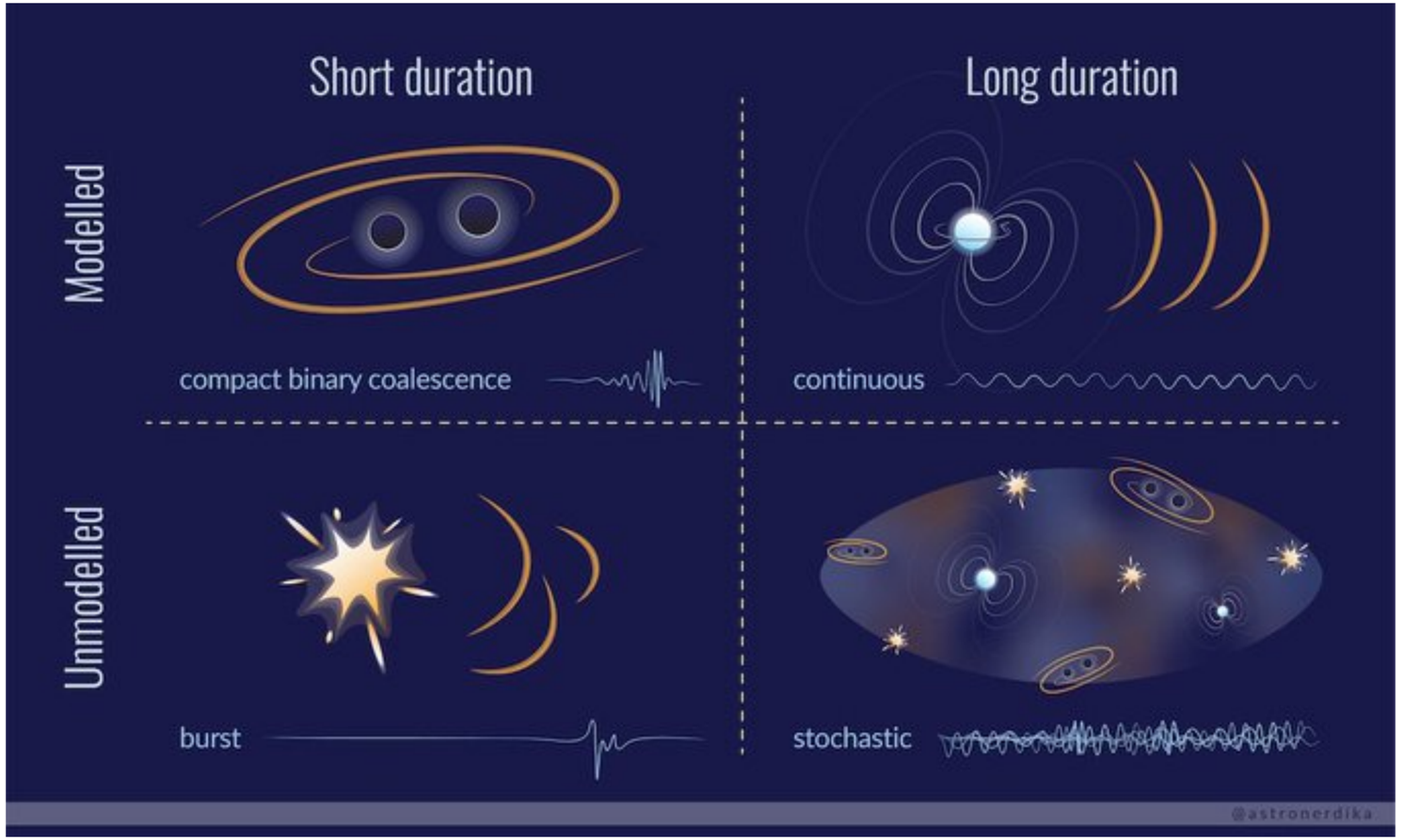

Source: https://www.spaceaustralia.com/news/cosmic-lighthouses-and-continuous-gravitational-waves

Predictions for Detection

$$\Omega_{\rm GW}(f) = \frac{f}{\rho_c}\frac{d\rho_{\rm GW}}{df}$$

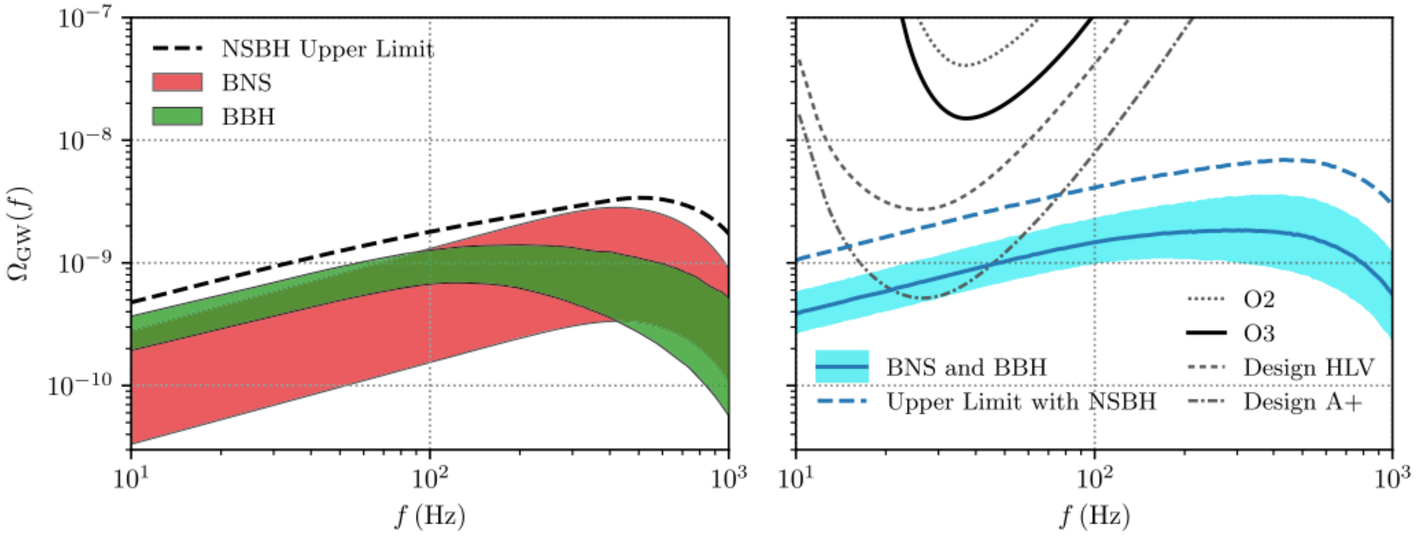

FIG. 5. Fiducial model predictions for the GWB from BBHs, BNSs, and NSBHs, along with current and projected sensitivity curves. In the left panel we show 90% credible bands for the GWB contributions from BNS and BBH mergers. Whereas the BNS uncertainty band illustrates purely the statistical uncertainties in the BNS merger rate, the BBH uncertainty band additionally includes systematic uncertainties in the binary mass distribution, as described in the main text. As no unambiguous NSBH detections have been made, we only show an upper limit on the possible contribution from such systems. The right panel compares the combined BBH and BNS energy density spectra, and 2σ power-law integrated (PI) curves for O2, O3, and projections for the HLV network at design sensitivity, and the A + detectors. The solid blue line shows the median estimate of $\Omega_{\rm BBH+BNS}(f)$ as a function of frequency, while the shaded blue band illustrates 90% credible uncertainties. The dashed line, meanwhile, marks our projected upper limit on the total GWB, including our upper limit on the contribution from NSBH mergers.

$$\bar{\Omega}_{\rm gw}(f_o) = \frac{8\pi G f_o}{3H_0^3 c^2}\int dz \int d\mathcal{M}_c \, \frac{R_{\rm merge}(\mathcal{M}_c, z)}{(1+z)\, h(z)}\frac{dE}{df}(f_e(z)|\mathcal{M}_c)\int_0^{\bar{\rho}} d\rho \, P_\rho(\rho|\mathcal{M}_c, z)\,,$$

PHYSICAL REVIEW D 104, 022004 (2021)

Is Intensity sky really isotropic?

Or Anisotropic ?

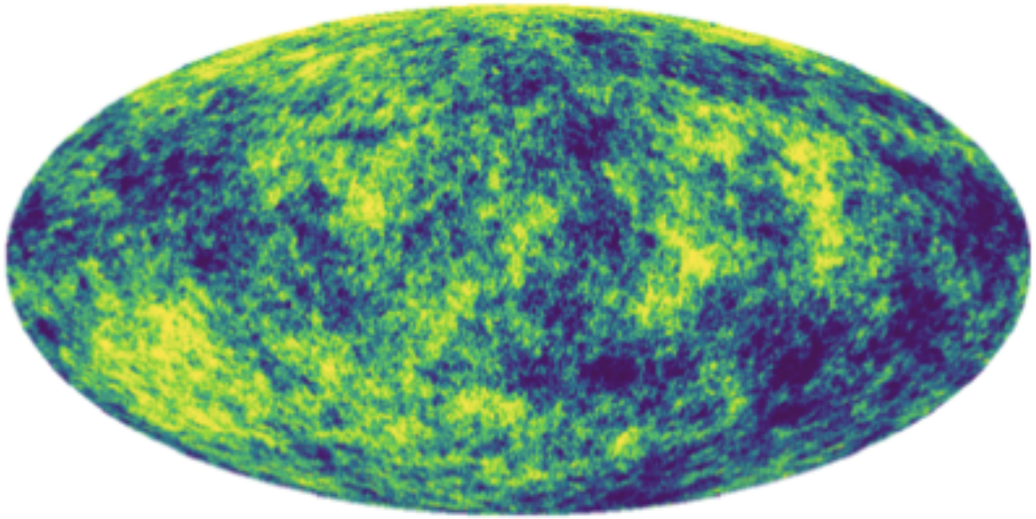

Credit: Alexander C. Jenkins

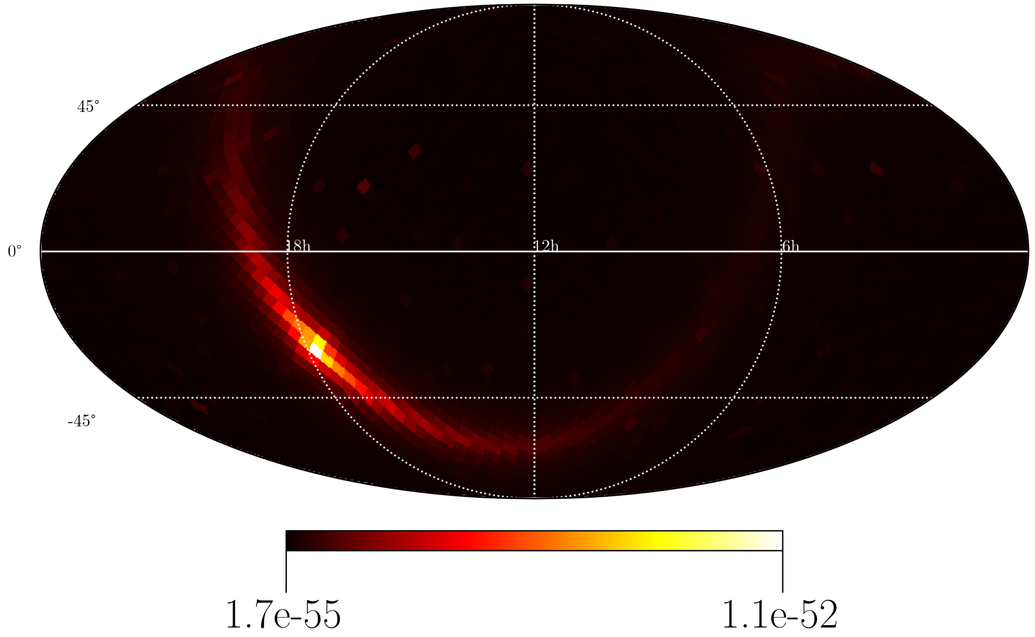

Reasons of Anisotropy

Cusin+ PRD 96, 103019 (2017)

- Astrophysical sources are located in cosmic structure and may produce anisotropic background.
  - Different mechanism of GW production
  - Astrophysical distribution of sources in galaxies
  - Galaxy Formation and Large scale structure distribution
  - Spacetime geometry along line of sight
- Point-like (hot spot) and extended anisotropy

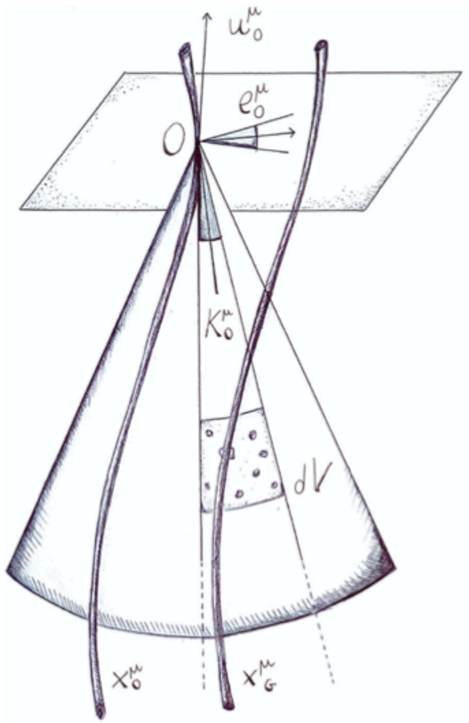

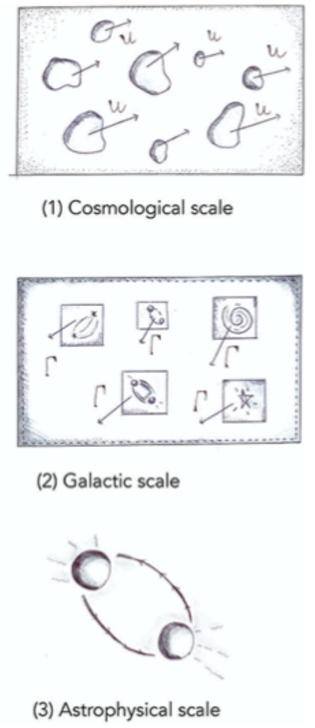

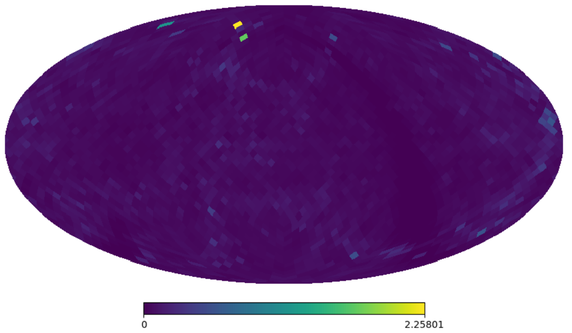

Chracterization of SGWB

A collection of unresolvable sub-threshold astrophysical and cosmological sources may produce SGWB.

- Gaussian
- Unpolarised
- Stationary
- Anisotropic

$$\langle \tilde{h}^{*}_{A}(f,\hat{n})\,\tilde{h}_{A'}(f',\hat{n}')\rangle \propto \delta_{AA'}\,\delta(f-f')\,\delta^{2}(\hat{n}-\hat{n}')\,\mathscr{P}_{A}(f,\hat{n})$$

Source PSD

Detection Strategy : GW Radiometer

Ballmer 2006

Mitra+ 2008

Thrane+2009

- GW signal is assumed to be correlated, but detector noise is not.
- $\langle \hat{C}_{12} \rangle = \langle d_1 d_2 \rangle = \langle h^2 \rangle + \langle h n_1 \rangle + \langle h n_2 \rangle + \langle n_1 n_2 \rangle$

Signal and noise uncorrelated

Noise Uncorrelated

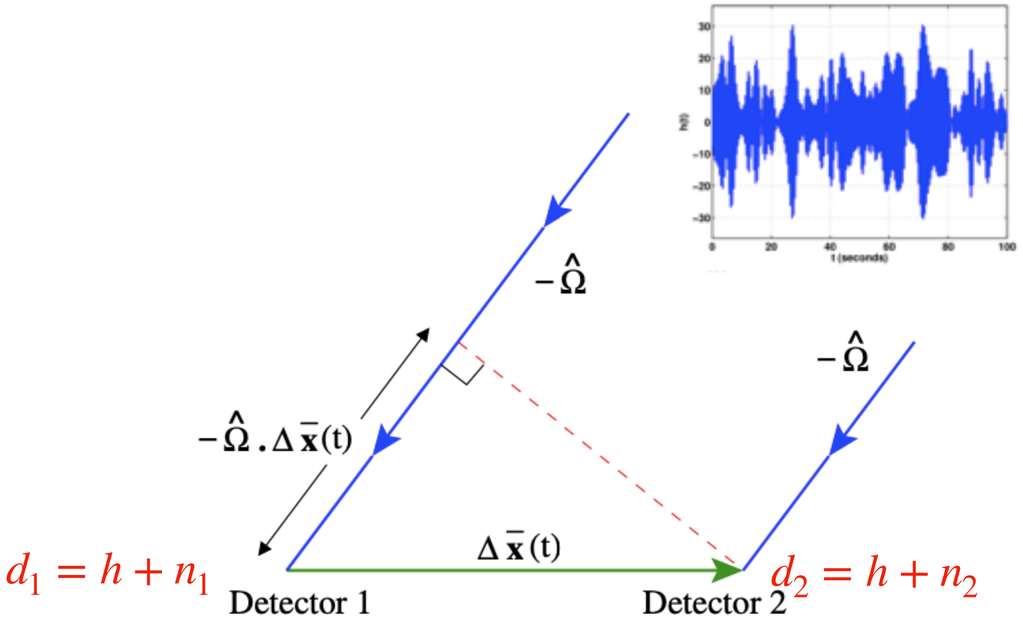

Mitra+ 2008

Detectors' Response to Background

- Cross Spectral Density:

$$\langle C^I(t;f)\rangle = \langle \tilde{d}_1^*(t;f)\,\tilde{d}_2(t;f)\rangle \propto \gamma_p^I(t,f)\,\mathscr{P}_p(f)$$

Detector's response

Observation

Source

- Overlap Reduction Function

$$\gamma_p^I(t,f) = \int d^2\hat{n}\,\left[(F_{1+}(t,\hat{n})F_{2+}(t,\hat{n}) + F_{1\times}(t,\hat{n})F_{2\times}(t,\hat{n})\right]\, e_p(\hat{n})\, e^{i2\pi f \frac{\hat{n}\cdot\Delta x_I(t)}{c}}$$

Basis for Sky Discretisation

Point Source $e_p(\hat{n}) = \delta^2(\hat{n} - \hat{n}_p)$

Extended Source $e_p(\hat{n}) = Y_{lm}(\hat{n})$

Overlap Reduction Function

Accounting Geometric Time Delay

$$\gamma_p^I(t,f) = \int d^2\hat{n}\ \left[(F_{1+}(t,\hat{n})F_{2+}(t,\hat{n}) + F_{1\times}(t,\hat{n})F_{2\times}(t,\hat{n})\right]\ e_p(\hat{n})\, e^{i2\pi f \frac{\hat{n}\cdot\Delta x_I(t)}{c}}$$

Real Part of ORF for HLVKI Network Changing with time

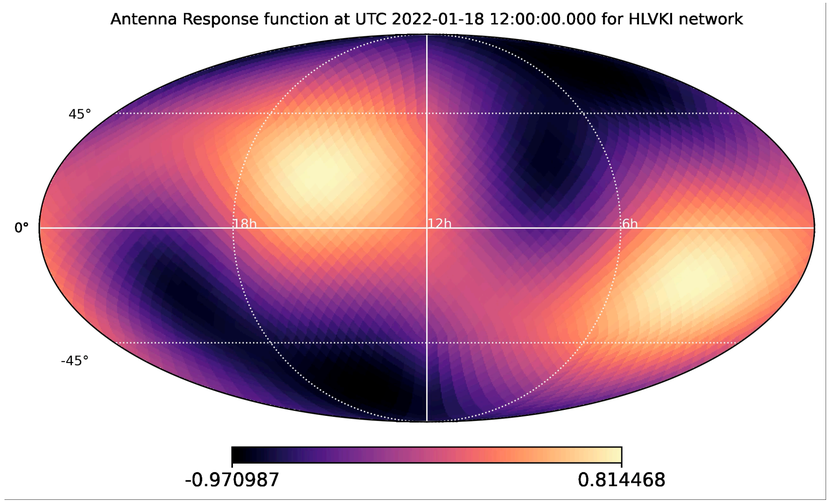

Real Part of ORF for HL Network as a function of frequency

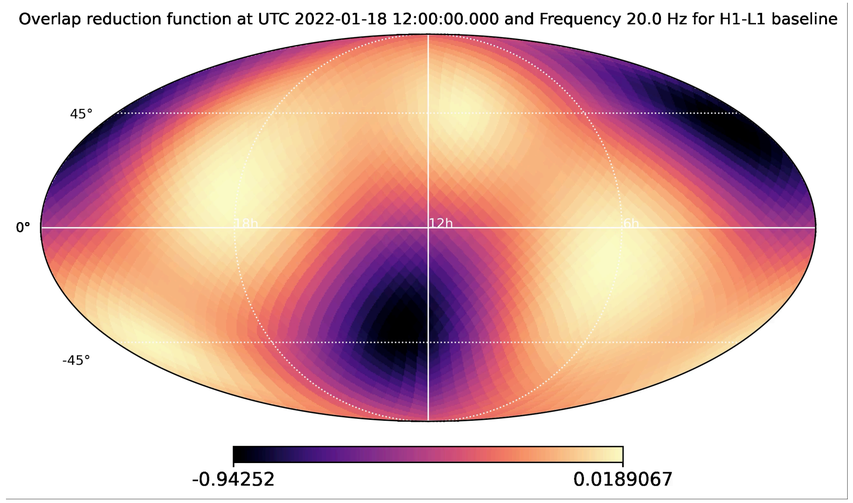

Credit : Jishnu Suresh

Narrowband Map-making

- Additive Gaussian Noise Likelihood and combining data from multiple baselines and time segments

$$-2\ln\mathscr{L} \propto \sum_{It} \frac{|\,C^I(t;f) - \gamma_p^I(t,f)\,\mathscr{P}_p(f)\,|^2}{P_1(t;f)\,P_2(t;f)}$$

- Clean Map $\boxed{\hat{\mathscr{P}}_p(f) = \Gamma^{-1}_{pp'}(f)\,X_{p'}(f)}$

- Dirty Map $X_p(f) \propto \mathscr{R}\left[\sum_{It} \frac{C^I(t;f)\,\gamma_p^{I*}(t;f)}{P_1(t;f)\,P_2(t;f)}\right]$

- Fisher Information Matrix $\Gamma_{pp'}(f) \propto \mathscr{R}\left[\sum_{It} \frac{\gamma_p^I(t:f)\,\gamma_{p'}^{I*}(t:f)}{P_1(t;f)\,P_2(t;f)}\right]$

Broadband Map-making

- Decomposing spatial and spectral dependence defined by power law with spectral index α

$$\mathscr{P}_p(f) = H(f)\,\mathscr{P}_p \qquad H(f) = \left(\frac{f}{f_{\rm ref}}\right)^{\alpha-3}$$

- Clean Map

$$\hat{\mathscr{P}}_p = \Gamma^{-1}_{pp'} X_{p'}$$

Deconvolution Problem

- Dirty Map

$$X_p = \sum_f H(f) X_p(f)$$

Narrowband Dirty Map & FIM

- Fisher Information Matrix

$$\Gamma_{pp'} = \sum_f H^2(f) \Gamma_{pp'}(f)$$

My Past Activities

Narrowband Search

Broadband Search

Phys. Rev. D105 122001 (2022)

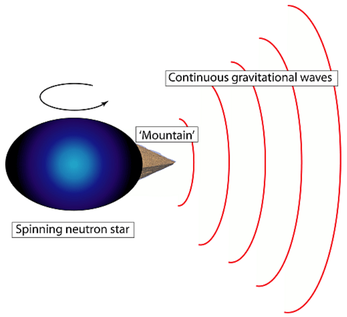

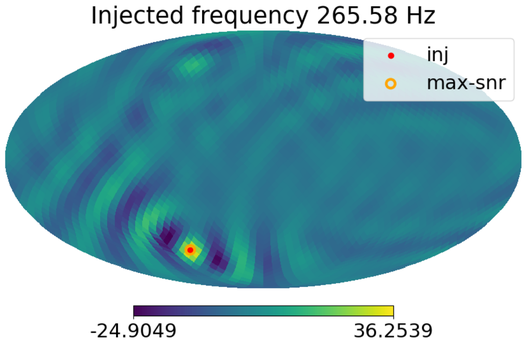

My Past Activities

Narrowband Search

Phys. Rev. D105 122001 (2022)

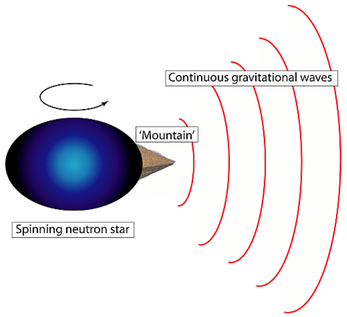

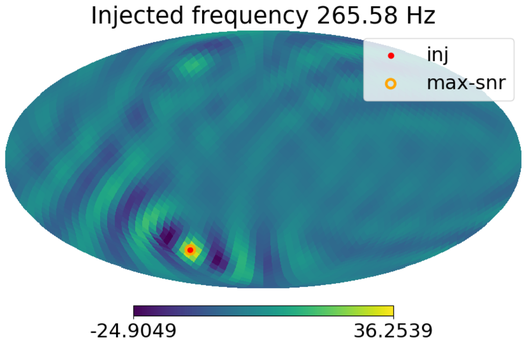

Broadband Search

Phys. Rev. D108 023011 (2023)

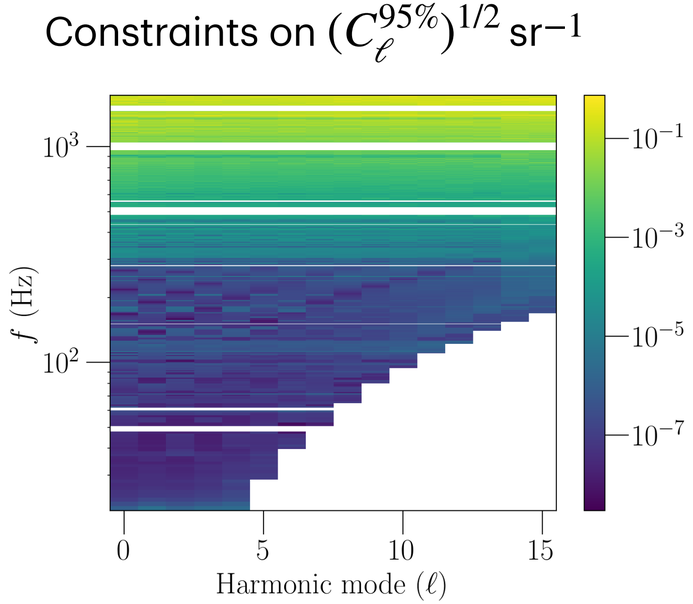

My Past Activities

Narrowband Search

Phys. Rev. D105 122001 (2022)

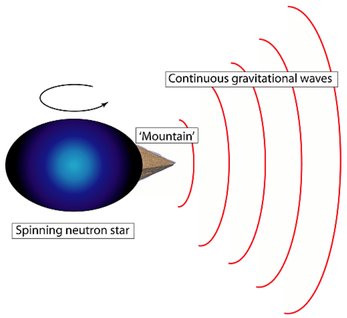

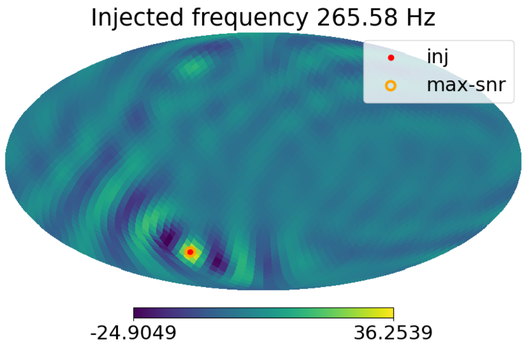

Phys. Rev. D108 023011 (2023)

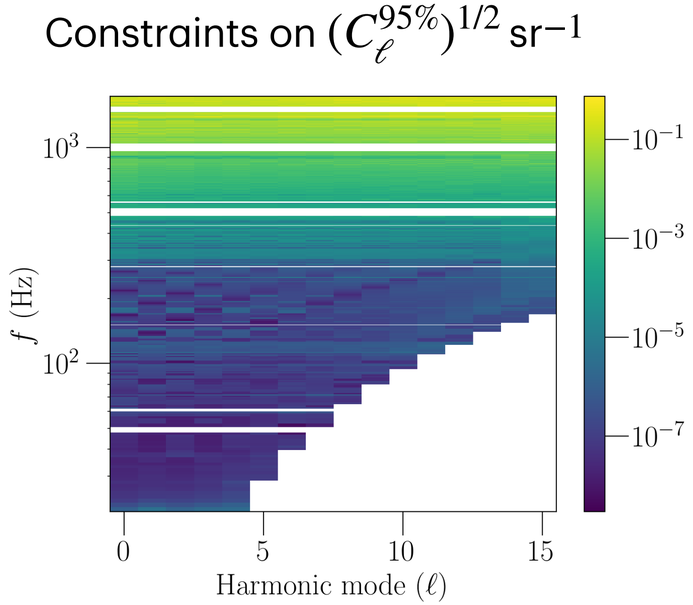

Broadband Search

Phys. Rev. D104 123018 (2021)

Inversion Problem

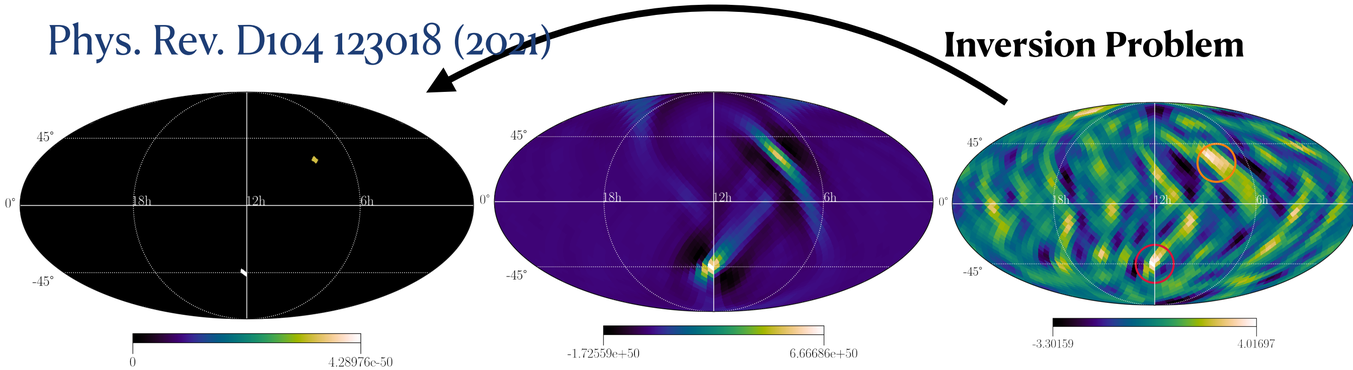

My Past Activities

Narrowband Search

Phys. Rev. D105 122001 (2022)

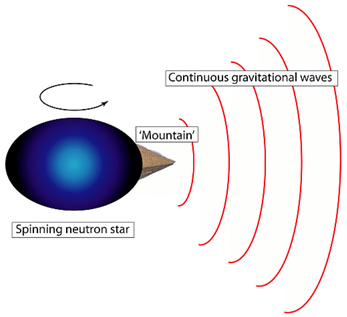

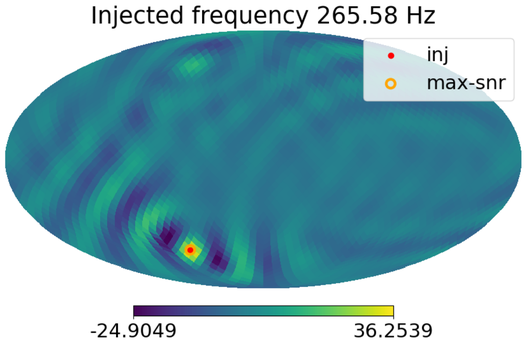

Phys. Rev. D108 023011 (2023)

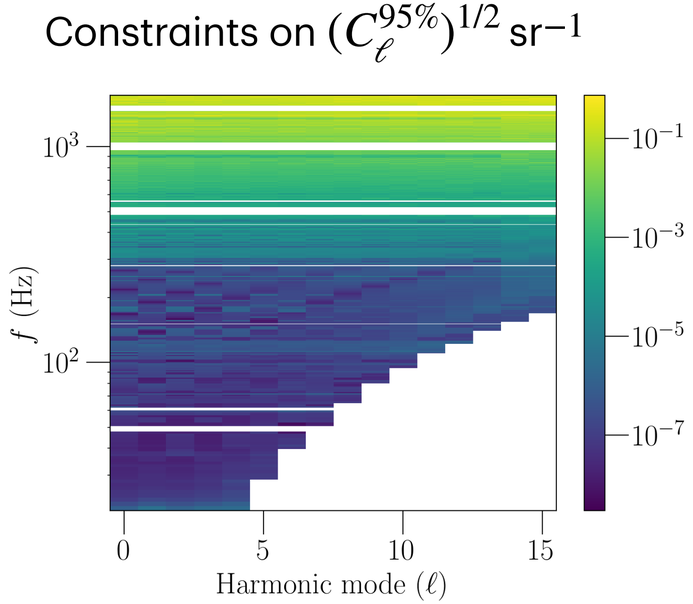

Broadband Search

Phys. Rev. D104 123018 (2021)

Inversion Problem

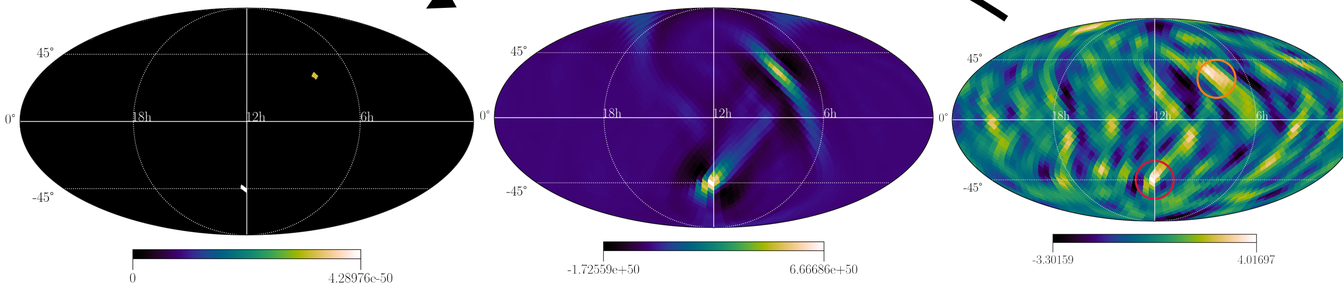

Component Separation

Phys. Rev. D104 102003 (2021)

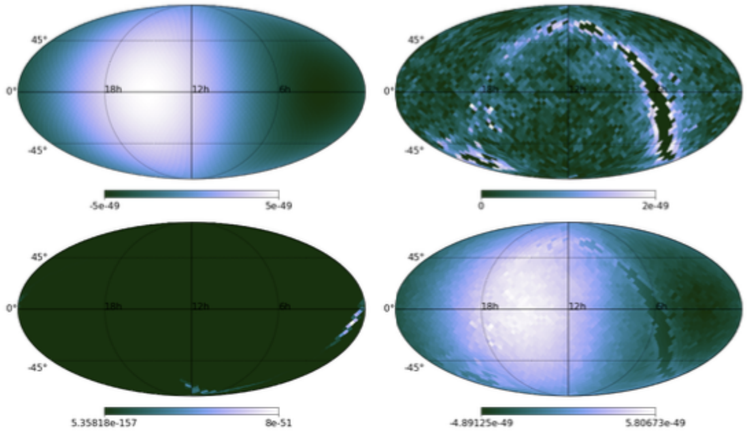

Targeted Search

Phys. Rev. D106 043019 (2022)

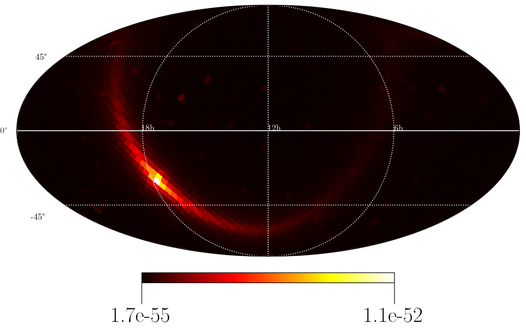

Narrowband Anisotropy

- Known Pulsars
- Unknown Neutron Stars
- Accreting neutron Stars in low-mass X-ray binaries

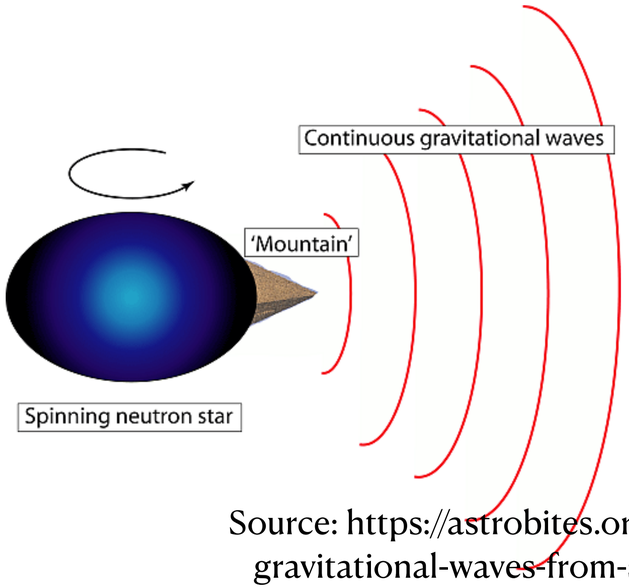

Source: https://astrobites.org/2018/01/29/hunting-for-gravitational-waves-from-spinning-neutron-stars/

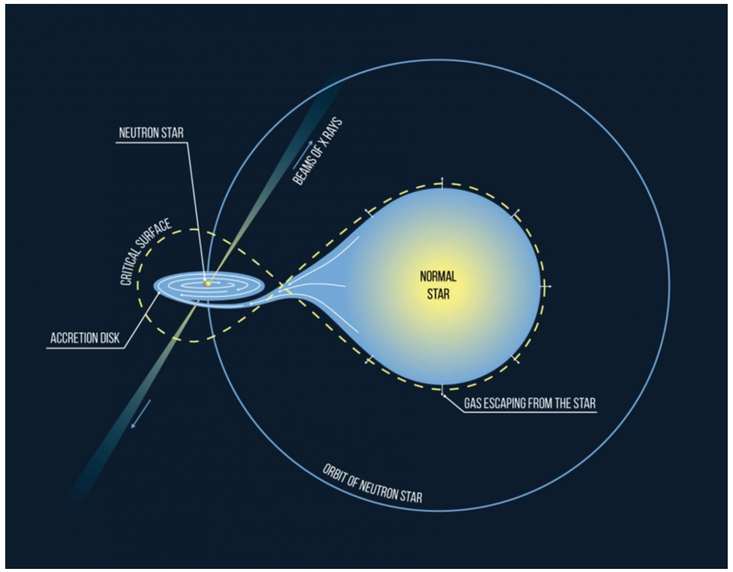

Source: https://www.spaceaustralia.com/news/cosmic-lighthouses-and-continuous-gravitational-waves

DA as part of LVK collaboration Phys. Rev. D105 122001 (2022)

ASAF: Point Sources

O2 Hardware Injection (HWI) Study

- 9 HWI like isolated neutron stars.
- 8 injections were detected within diffraction limited sky region and in the nearest frequency bin to injection.
- 1 weak injection was classified as follow up candidate.

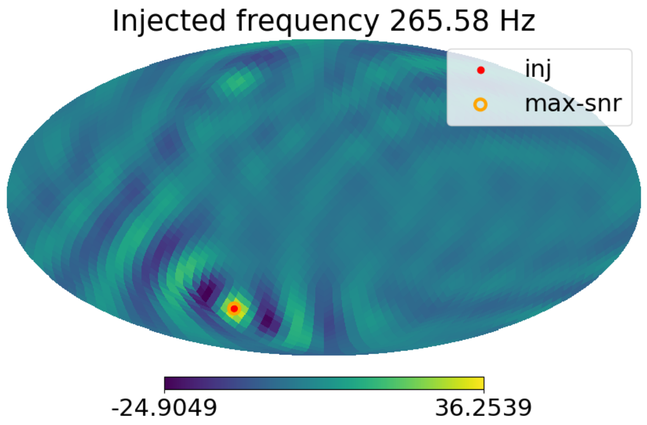

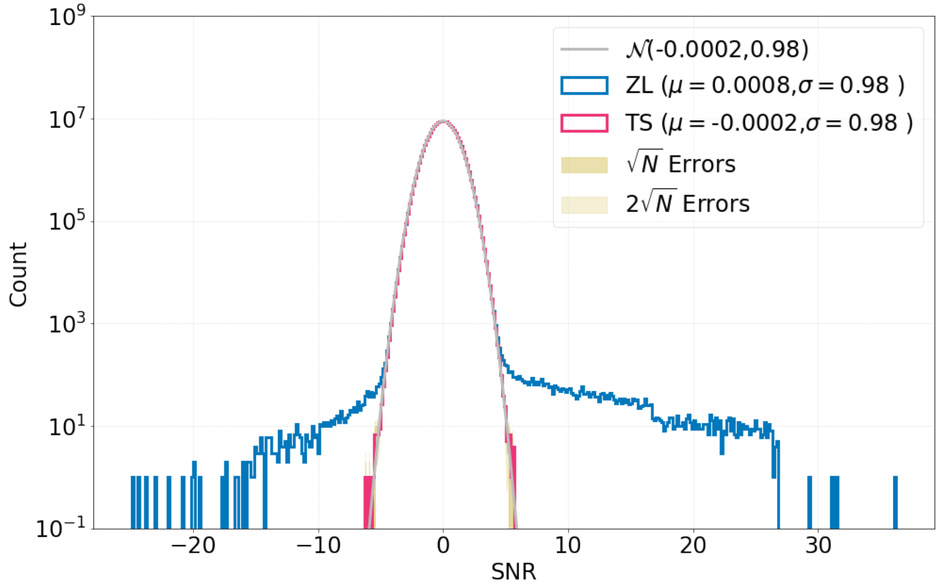

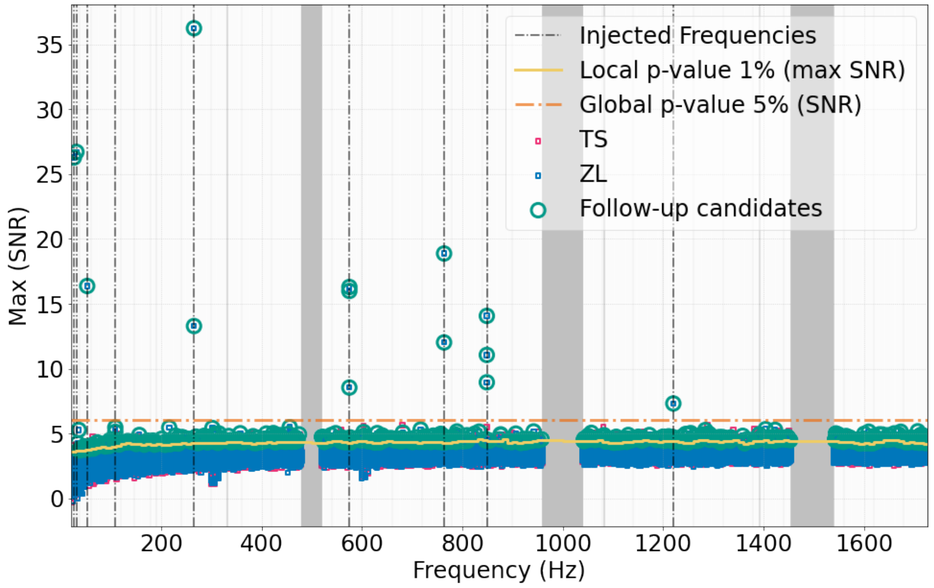

ASAF : Point Sources

O1+O2+O3 (HLV) Real Data

DA as part of LVK collaboration Phys. Rev. D105 122001 (2022)

- No significant outlier for anisotropic narrowband source.
- 515 sub-threshold candidates identified for CW follow up.

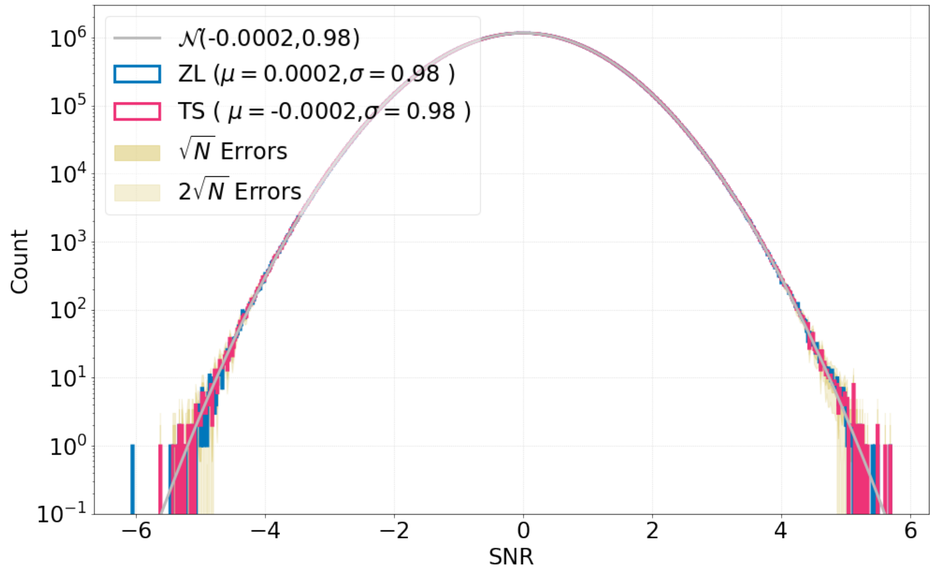

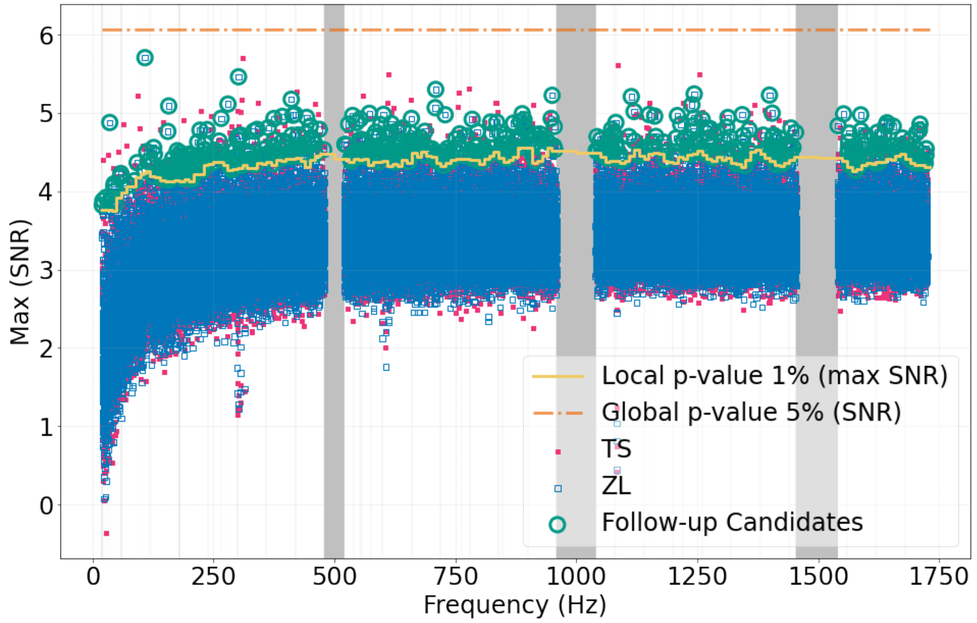

ASAF : Point Sources

O1+O2+O3 HLV data

- Upper limits lie in range $h_{0,eff} \leq (0.030 - 9.6) \times 10^{-24}$.
- Bayesian upper limit with 95% confidence.
- Marginalization on calibration uncertainty.
- Uniform prior on the effective strain.

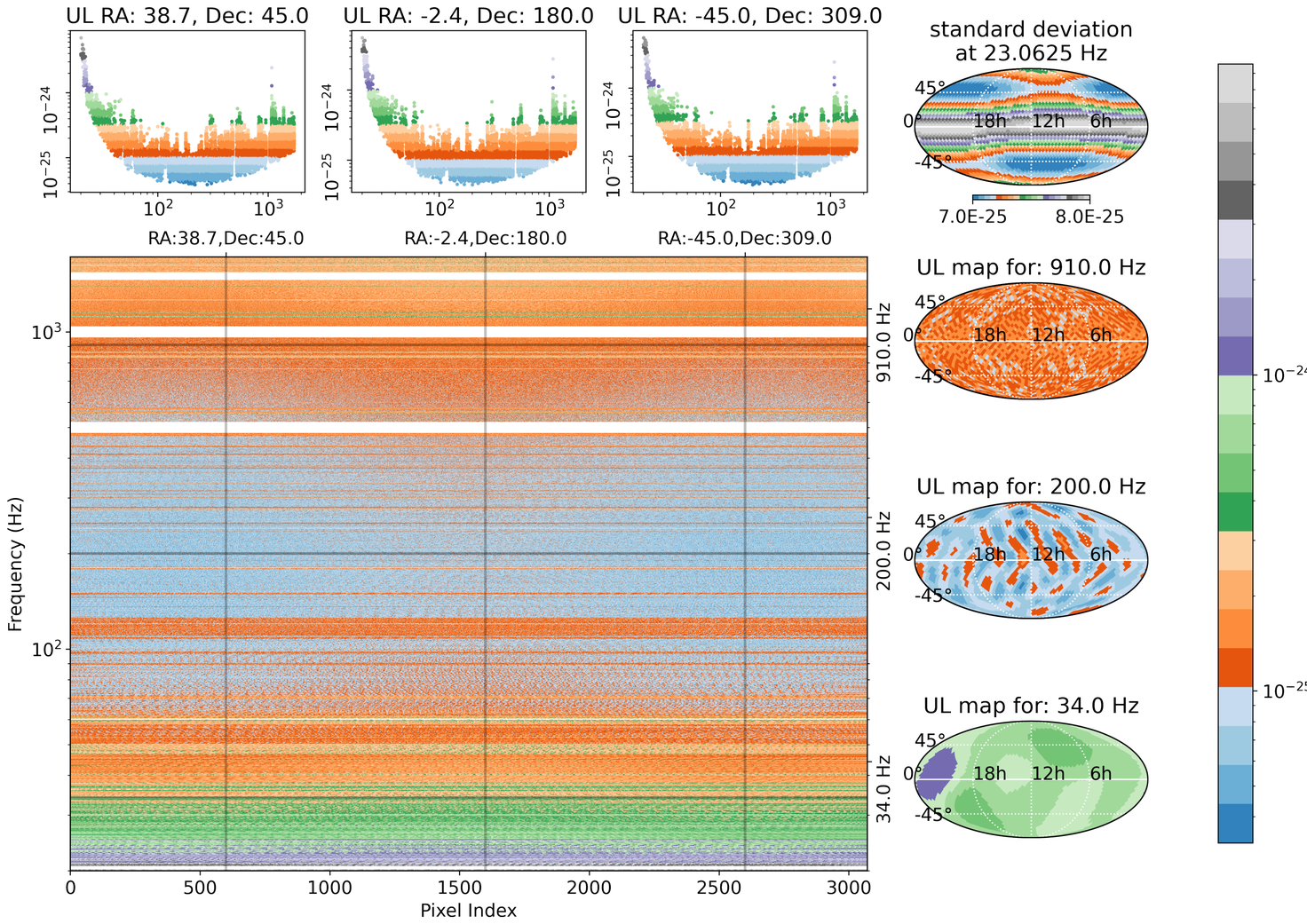

ASAF: Extended Sources

DA, J. Suresh, S. Mitra and A. Ain. arXiv:2302.12516 [gr-qc]

A statistically isotropic Gaussian Anisotropy can be characterised by mean and variance.

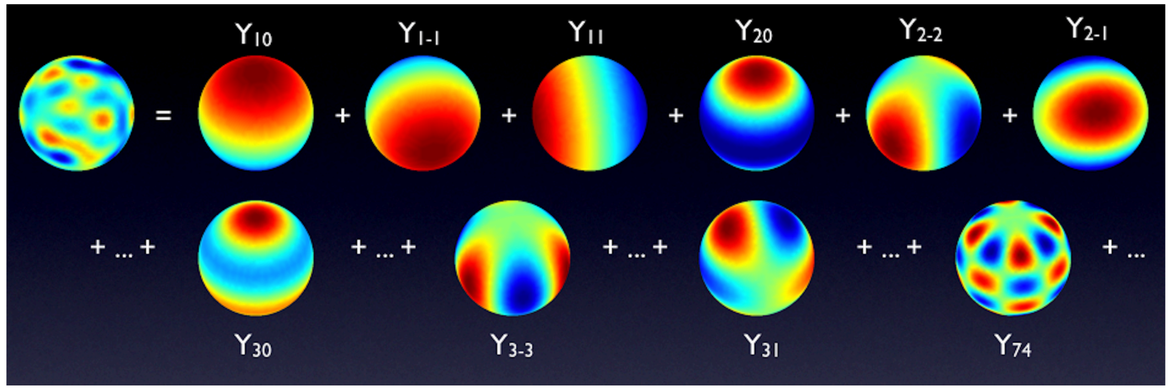

doi: https://doi.org/10.1371/journal.pone.0044439.g012

- Average over universe realisations

$$\langle \mathscr{P}_{\ell m}(f) \rangle_U = \sqrt{4\pi}\, \bar{\mathscr{P}}(f)\, \delta_{\ell 0}$$

Monopole Term

- Variance Term

$$\mathrm{Cov}[\mathscr{P}_{\ell m}(f)\mathscr{P}_{\ell' m'}(f)]_U = \left(\frac{2\pi^2 f^3}{3H_0^2}\right)^{-2} C_\ell(f)\, \delta_{\ell\ell'}\, \delta_{mm'}$$

Narrowband Angular Power Spectrum

ASAF: Extended Sources

MLE and Angular power Spectrum

$$\hat{C}_\ell(f) = \left(\frac{2\pi^2 f^3}{3H_0^2}\right)^2 \frac{1}{2\ell+1} \sum_m \left[|\hat{\mathscr{P}}_{\ell m}(f)|^2 - \left[\mathbf{\Gamma}_R^{-1}\mathbf{\Gamma}\mathbf{\Gamma}_R^{-1}\right]_{\ell m,\ell m}(f) \right]$$

$$\hat{\mathscr{P}}_{\ell m}(f) = (\mathbf{\Gamma}_R^{-1})_{\ell m,\ell' m'}(f)\, X_{\ell' m'}(f)$$

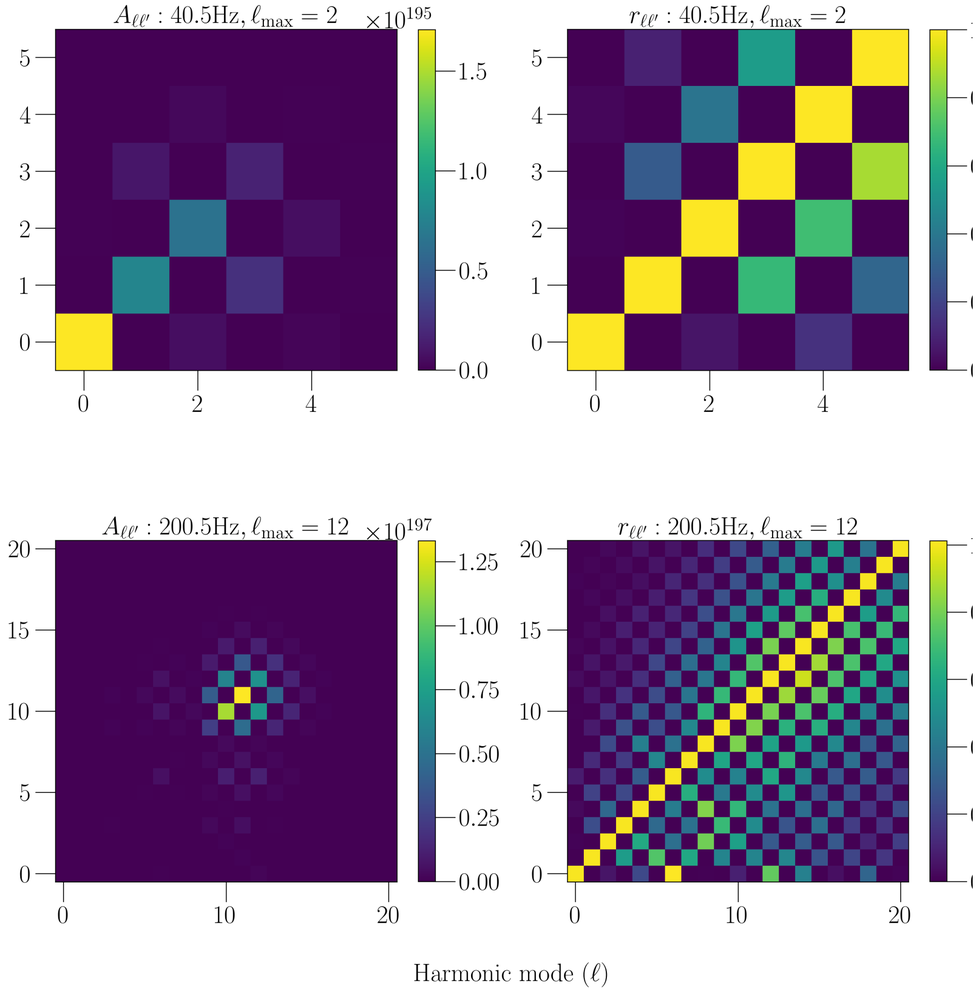

ASAF: Extended Sources

O3 HLV Data Significance

DA, J. Suresh, S. Mitra and A. Ain. arXiv:2302.12516 [gr-qc]

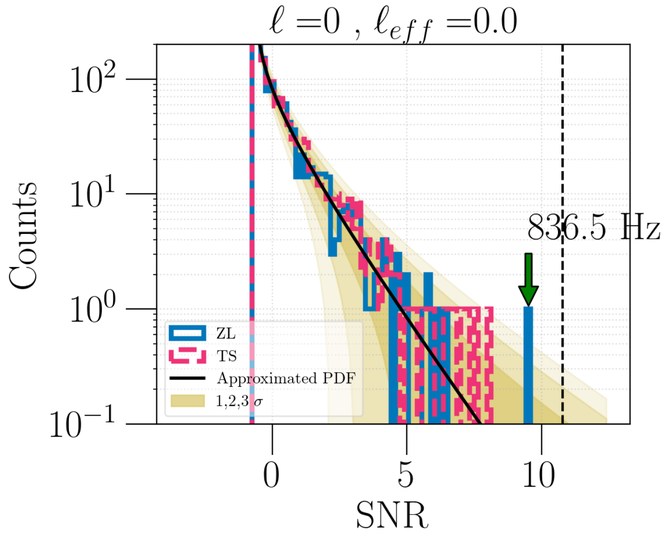

- We set $\ell_{max} = 15$.
- The null distribution for SNR is fitted with modified chi-squared distribution.

$$P(y = \rho_\ell(f))\, dy = \sqrt{2k}\, \chi^2_k(y\sqrt{2k} + k)\, dy$$

- The Data is found to be consistent with Noise.

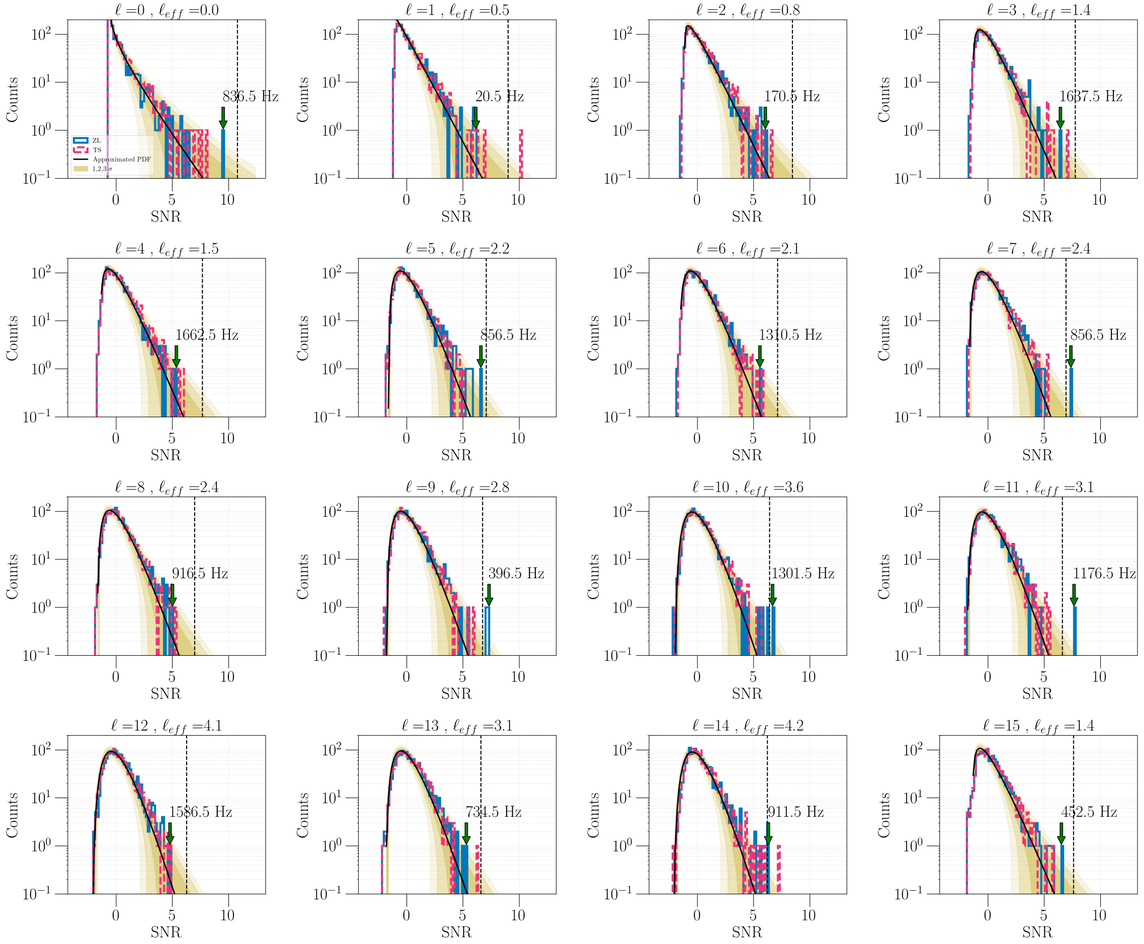

DA, J. Suresh, S. Mitra and A. Ain. arXiv:2302.12516 [gr-qc]

ASAF: Extended Sources

Constraints on $(C_\ell^{95\%})^{1/2}$ **sr**$^{-1}$

- Bayesian Upper limits with 95% confidence.
- Upper limits lie in range $C_\ell^{1/2} \leq (3.0 \times 10^{-9} - 0.73)\ \mathrm{sr}^{-1}$
- Consistent with the predictions!

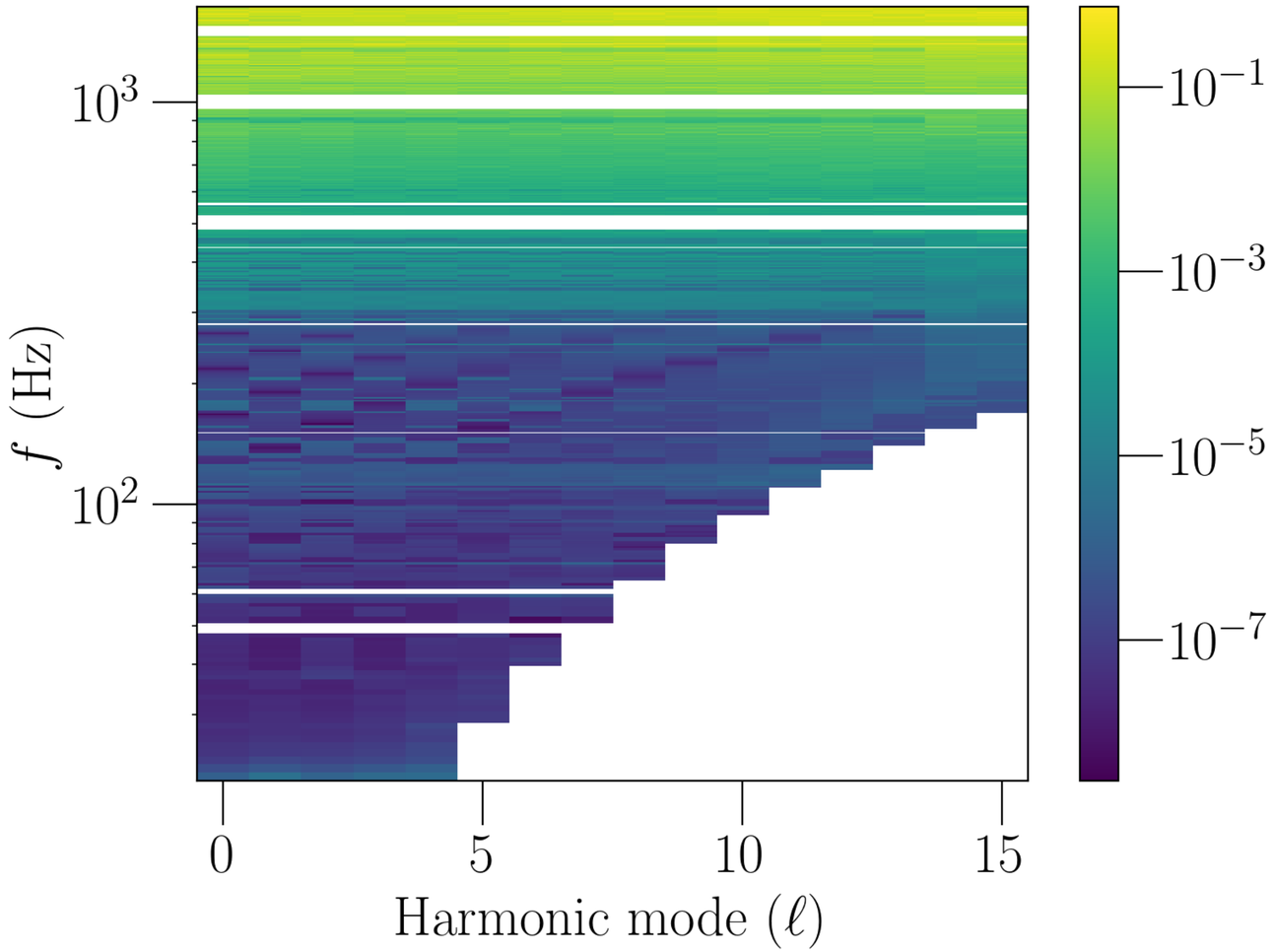

Broadband Anisotropy

Broadband SGWB Sources

$$\bar{\Omega}_{\rm gw}(f_{\rm o}) = \frac{8\pi G f_{\rm o}}{3H_0^3 c^2} \int dz \int d\mathcal{M}_c \, \frac{R_{\rm merge}(\mathcal{M}_c, z)}{(1+z)\, h(z)} \frac{dE}{df}(f_e(z)|\mathcal{M}_c) \int_0^{\bar{\rho}} d\rho \, P_\rho(\rho|\mathcal{M}_c, z)\,,$$

$$\frac{dE}{df} \simeq \frac{(\pi G)^{2/3}\mathcal{M}_c^{5/3}}{3} \times \begin{cases} f^{-1/3} & f < f_{\rm merg} \\ f_{\rm merg}^{-1} f^{2/3} & f_{\rm merg} \leq f < f_{\rm ring} \\ \dfrac{f_{\rm merg}^{-1} f_{\rm ring}^{-4/3} f^2}{\left[1 + \left(\dfrac{f - f_{\rm ring}}{\sigma/2}\right)^2\right]^2} & f_{\rm ring} < f \leq f_{\rm cut} \end{cases} .$$

Credit: Alexander C. Jenkins

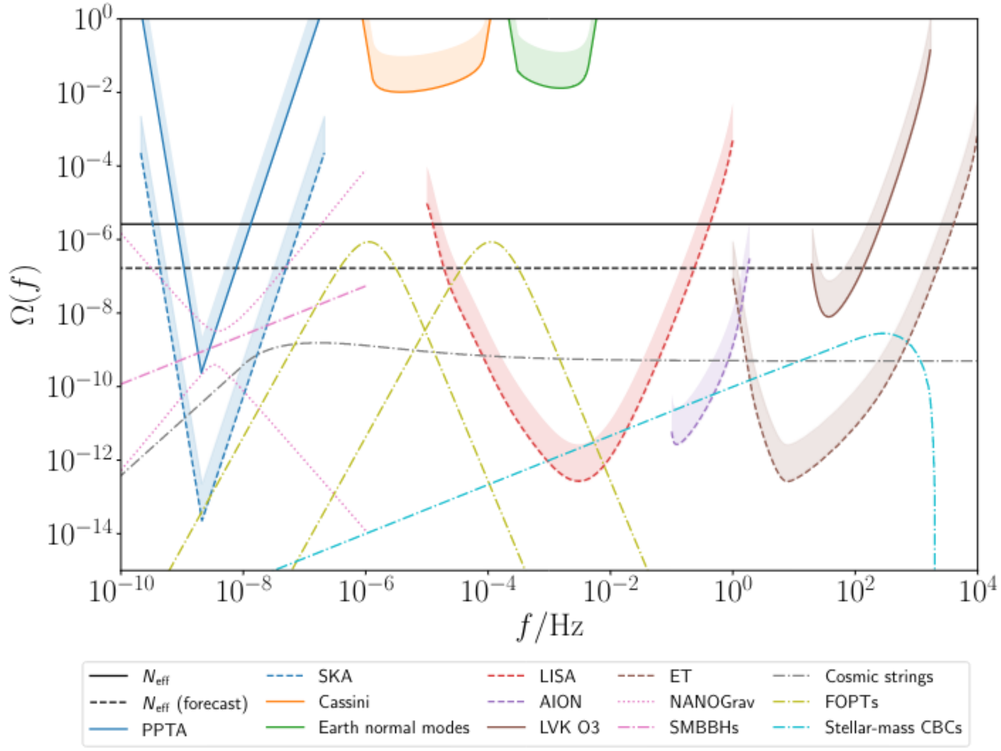

Broadband Map-making

DA, J. Suresh, S. Mitra and A. Ain. Phys. Rev. D104 123018 (2021)

- Decomposing spatial and spectral dependence defined by power law with spectral index α

$$\mathscr{P}_p(f) = H(f)\,\mathscr{P}_p \qquad H(f) = \left(\frac{f}{f_{\rm ref}}\right)^{\alpha-3}$$

- Clean Map

$$\hat{\mathscr{P}}_p = \Gamma^{-1}_{pp'} X_{p'}$$

Deconvolution Problem

- Dirty Map

$$X_p = \sum_f H(f) X_p(f)$$

Narrowband Dirty Map & FIM

- Fisher Information Matrix

$$\Gamma_{pp'} = \sum_f H^2(f) \Gamma_{pp'}(f)$$

Deconvolution Problem

DA, J. Suresh, S. Mitra and A. Ain. Phys. Rev. D104 123018 (2021)

- Observed Dirty Map
  $X_p = \Gamma_{pp'} \mathscr{P}_{p'} + n_p$
- MLE $\hat{\mathscr{P}}_p = \Gamma^{-1}_{pp'} X_{p'}$
- Regularization of matrix is required!

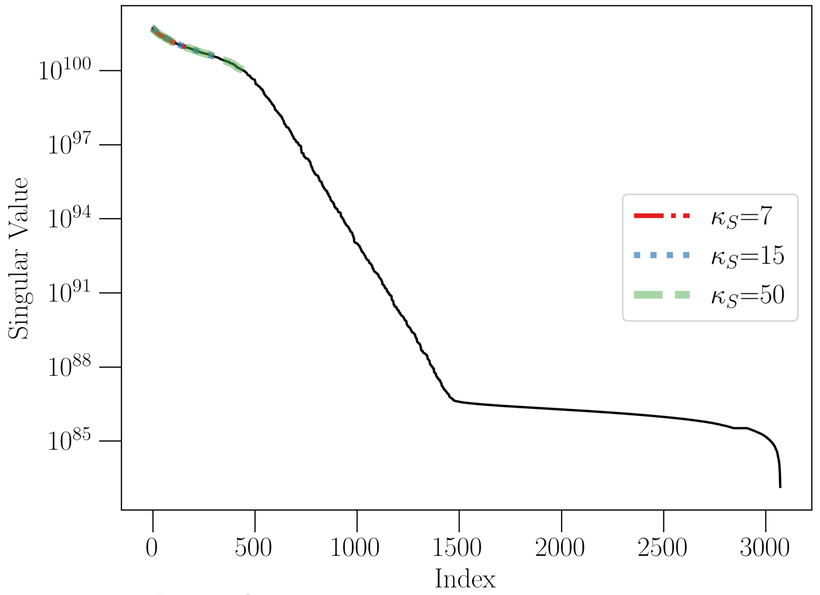

Bias-Variance Trade-off

Injected Point Source

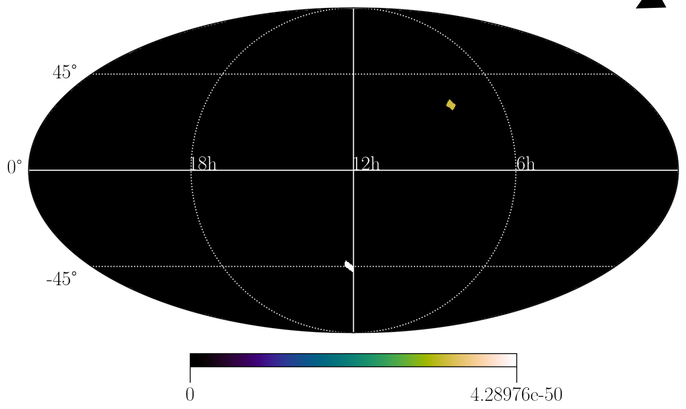

Dirty Map without Noise

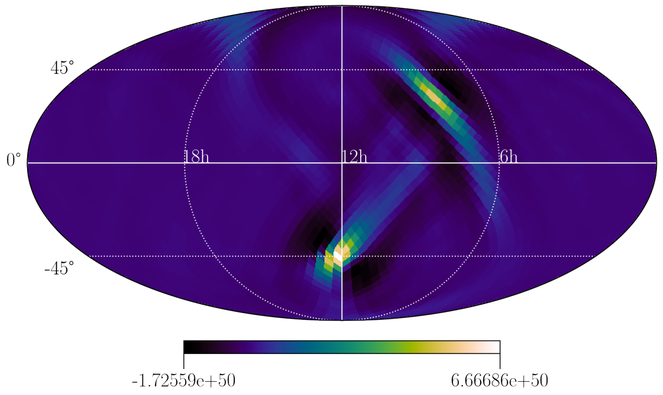

Dirty Map with Noise

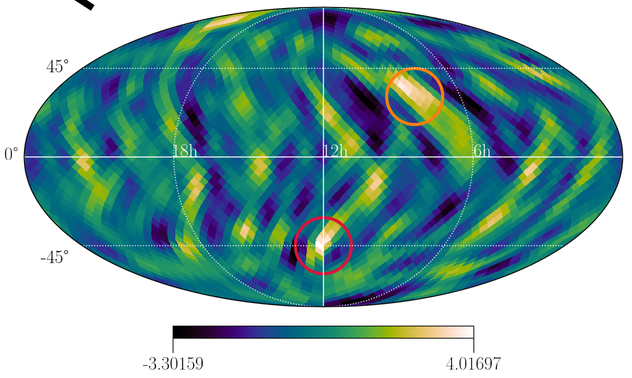

Effect of Regularisation

DA, J. Suresh, S. Mitra and A. Ain. Phys. Rev. D104 123018 (2021)

- SVD Regularisation $\Gamma' = U\Sigma' V^{\dagger}$
- Norm Regularisation $\Gamma' = \Gamma + \lambda I$
- Metric to estimate quality of inversion : NMSE

$$= \frac{||\text{Injection} - \text{Recovery}||}{||\text{Injection}||}$$

- Injection of SNR 3-4, $\alpha = 3$

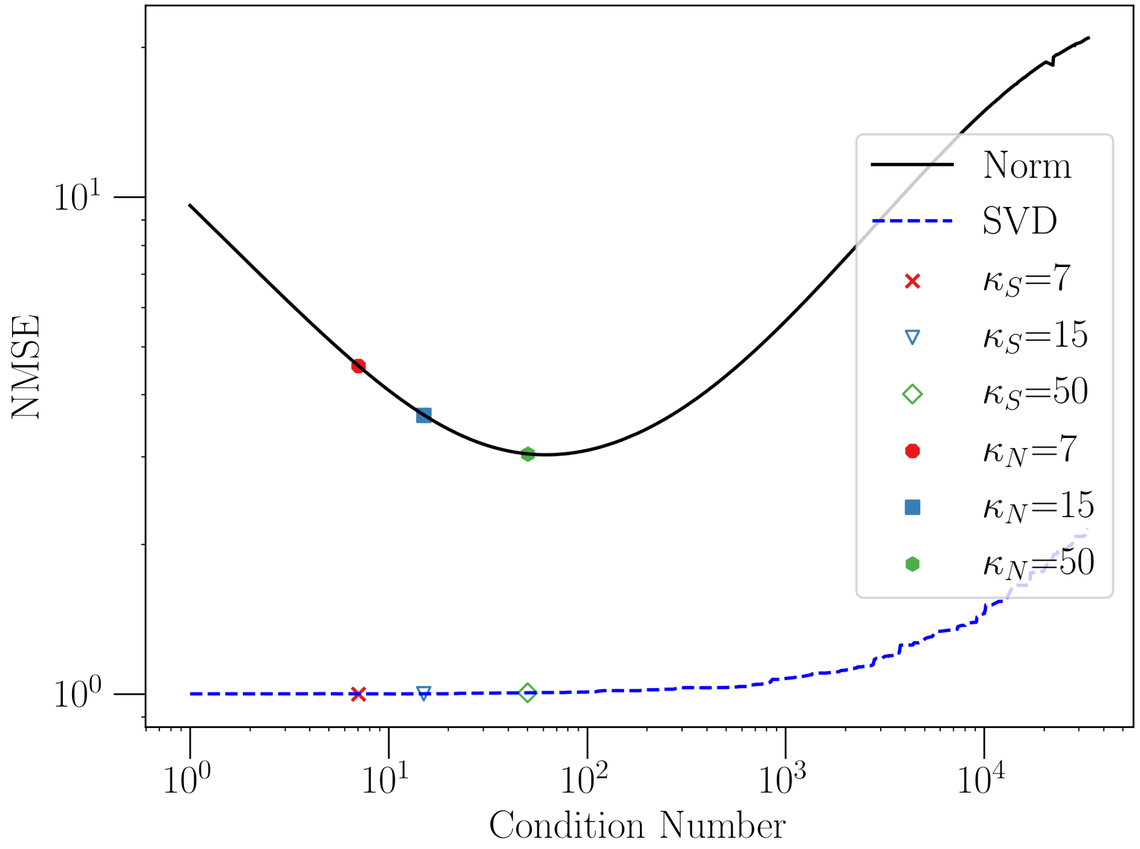

Effect on Significance

- Injection of realistic SNR 3-4,
- Computed p-value using regularized clean map and their covariance matrices.
- Compared with the standard Method.
- The norm regularised clean map with condition number 15 and the dirty map works better than SVD regularised clean map.

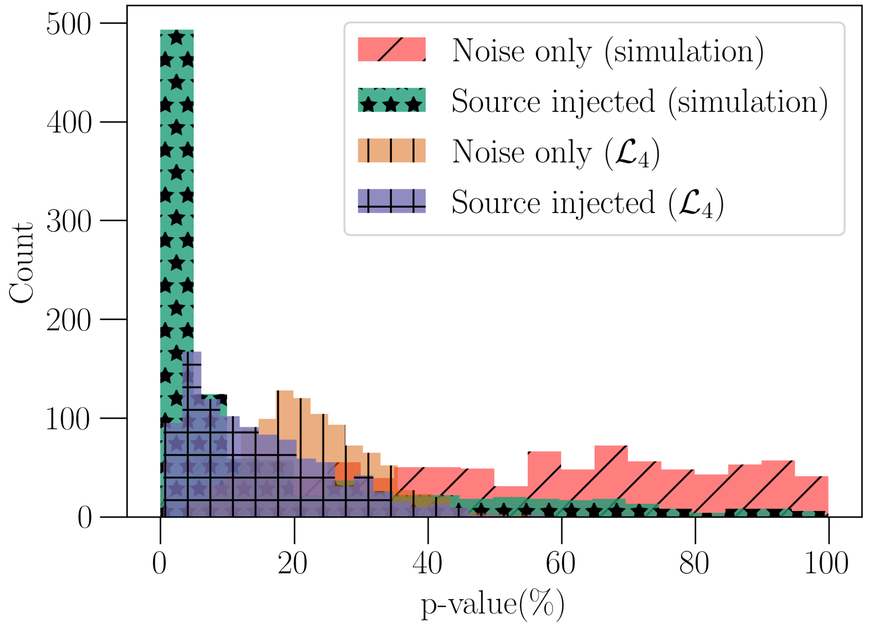

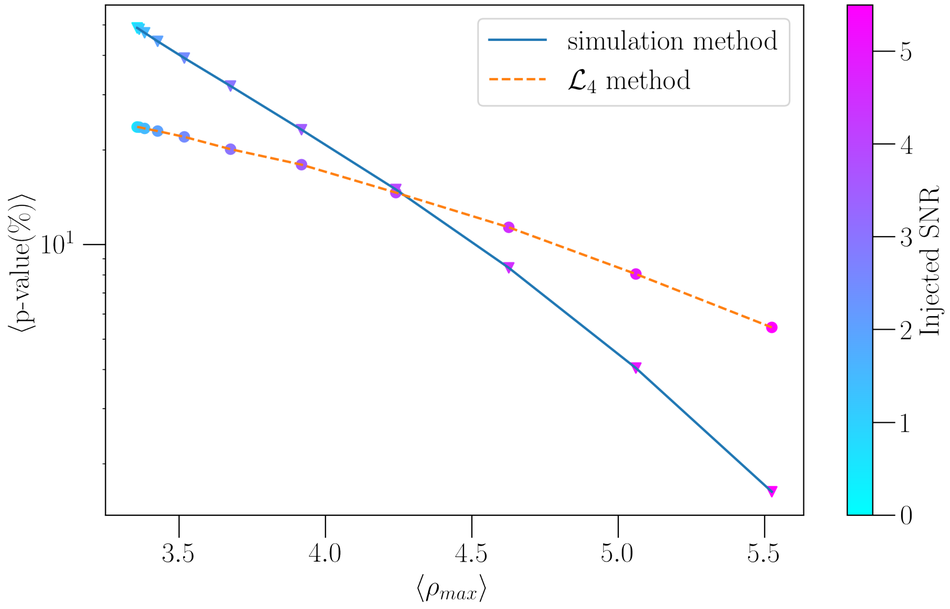

Effect on Upper Limits

DA, J. Suresh, S. Mitra and A. Ain. Phys. Rev. D104 123018 (2021)

- Injection with SNR~2.5 in each pixel of 3072 pixels in a map at a time.
- Upper limit comparison with Conventional method, Norm regularised clean map with diagonals of NCVM and full NCVM
- We can continue setting upper limits with conventional method.

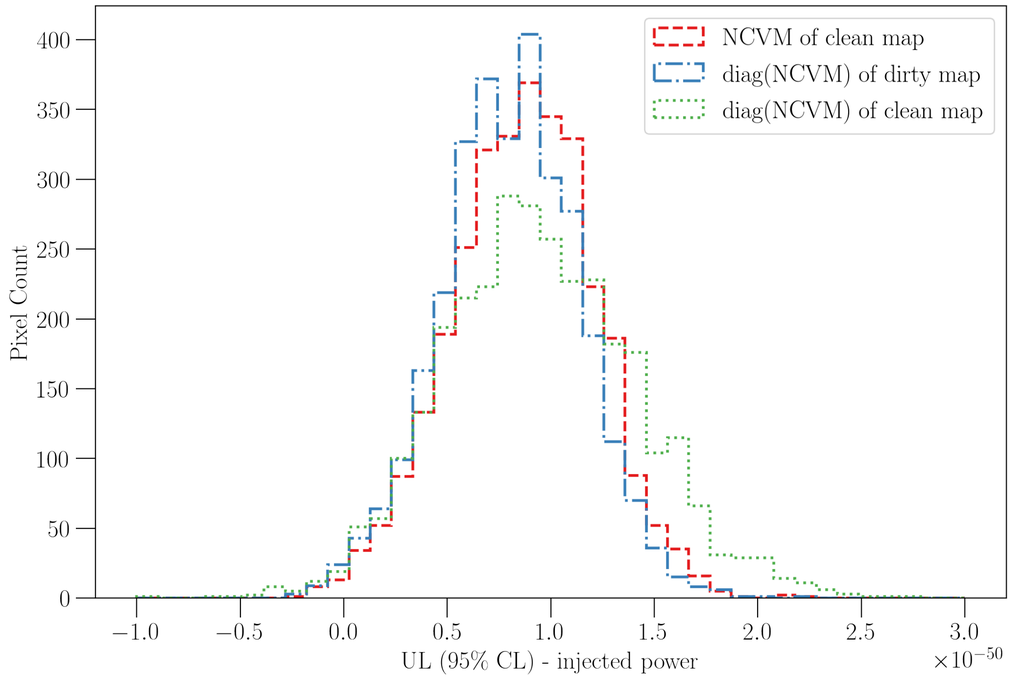

J. Suresh, **DA**, S. Mitra Phys. Rev. D104 102003 (2021)

Component Separation

- Estimates from searching for a source at a time might be biased (overestimated).
- But uncertainty increases as number of source population included in joint-estimation increase.

$$\langle \mathscr{C}^{\mathscr{I}} \rangle = \tau \sum_{\alpha} H_{\alpha}(f)\, \gamma^{I}_{ft,u}\, \mathscr{P}^{\alpha}_{u}$$

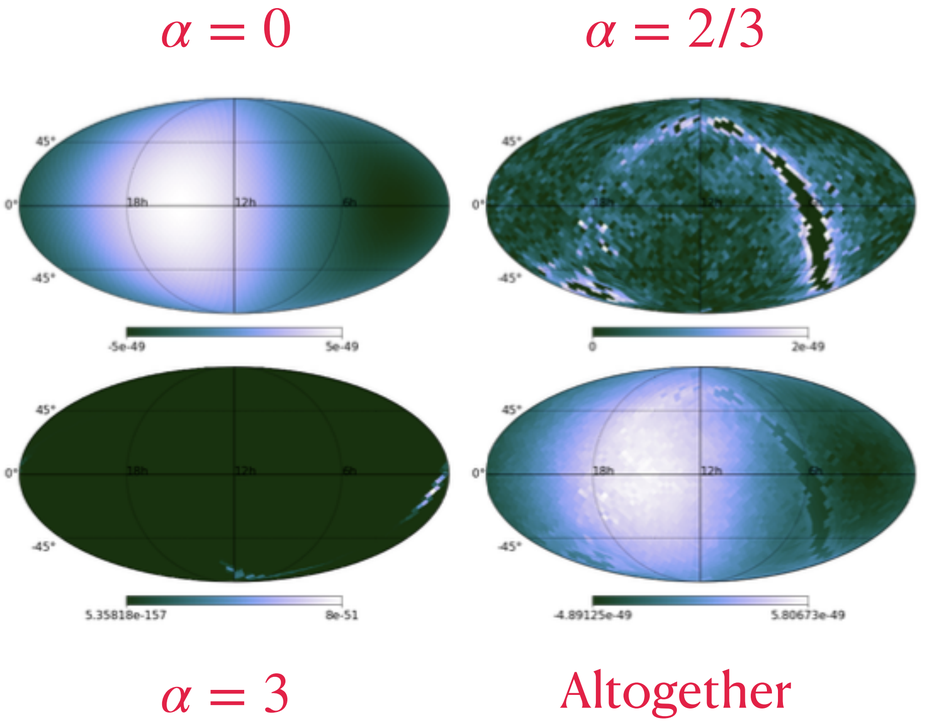

We observe the integrated effect of all sources.

Injection Study

J. Suresh, **DA**, S. Mitra Phys. Rev. D104 102003 (2021)

$$X \equiv X_u^\alpha = \sum_{Ift} \gamma_{ft,u}^{I*} \frac{H_\alpha(f)}{P_{\mathcal{J}_1}(t;f) P_{\mathcal{J}_2}(t;f)} \mathscr{C}^I(t;f)$$

$$\hat{\mathscr{P}}_u^\alpha \equiv \hat{\mathscr{P}} = \Gamma^{-1} \cdot X$$

$$\Gamma \equiv \Gamma_{uu'}^{\alpha\beta} = \sum_{Ift} \frac{H_\alpha(f) H_\beta(f)}{P_{\mathcal{J}_1}(t;f)\, P_{\mathcal{J}_2}(t;f)} \gamma_{ft,u}^{I*} \gamma_{ft,u'}^{I}$$

Dirty Map

SC clean map

MC clean map

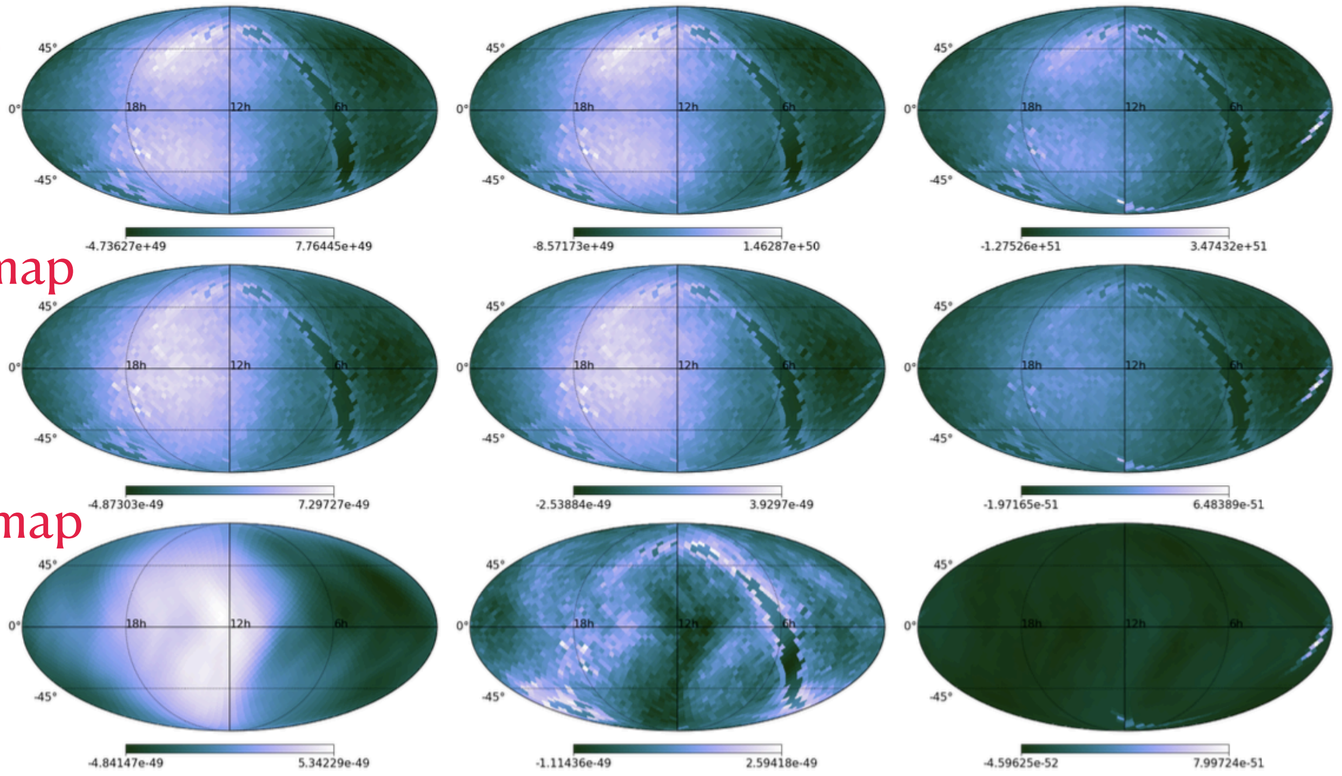

FIG. 3. Recovery of the injected source map using single index and multi-index estimations for $\alpha = 0, 2/3, 3$ from left to right. The first row shows the dirty maps obtained by the optimal filtering assuming a spectral shape. The second row shows the recovered semiclean map with the conventional single-index component separation. The third row depicts the semiclean map from a joint-index multicomponent analysis. All the maps are represented as a color bar plot on a Mollweide projection of the sky in ecliptic coordinates.

J. Suresh, **DA**, S. Mitra Phys. Rev. D104 102003 (2021)

Amplitude

Uncertainty

Upper Limits

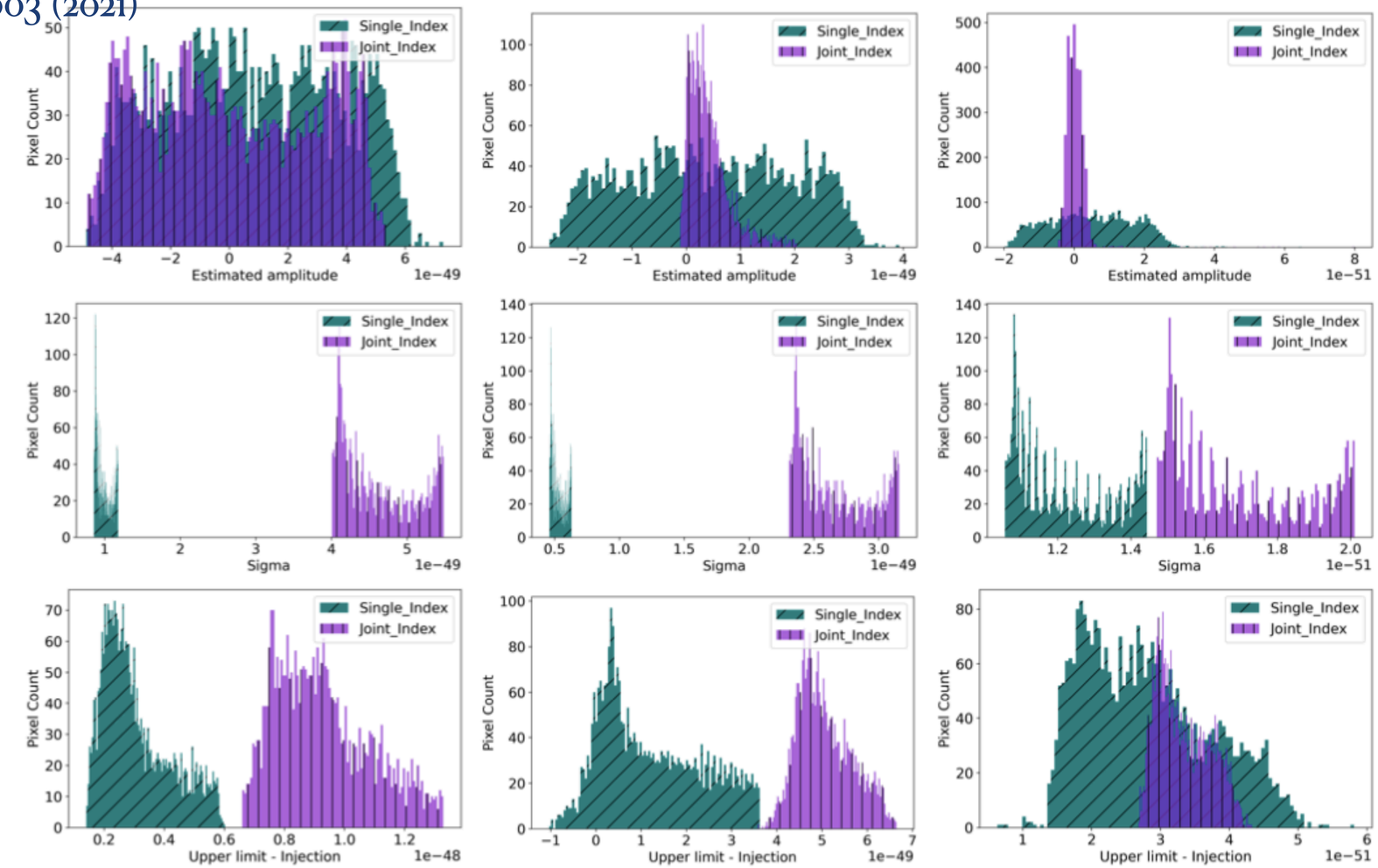

FIG. 5. Estimated amplitude and 95% upper limit along with the variance of the estimators from the injection study (with corresponding injection amplitudes of $5 \times 10^{-49}, 2 \times 10^{-49}$ and 8×10^{-51} respectively) is shown for $\alpha = 0, 2/3, 3$ from left to right respectively. In all the histograms, cyan (slant hatched) represents the single-index analysis and purple (vertical hatch) shows the joint-index analysis. Top panel histograms show the estimated amplitudes from both the methods. Middle panel depicts the variances of single-index and joint-index estimators. The bottom panel shows the differences between the estimated upper limits and the (high SNR) injections. For a valid 95% upper limit, the difference should be positive for more than $\sim 95\%$ pixels. However, this is not the case for the single index analysis for $\alpha = 2/3$, as seen in the middle column of the bottom panel, where $\sim 11\%$ of the pixels have negative differences.

Results from O1+O2+O3a HL data

J. Suresh, **DA**, S. Mitra Phys. Rev. D104 102003 (2021)

95% Upper Limit $\times 10^{-8}$					
α	Single Index	Joint Index			
		two-α			three-α
		0 , 2/3	0 , 3	2/3 , 3	
0	2.89-0.118	7.05-57.84	2.71-13.07		8.66-75.58
2/3	1.38-6.35	3.85-19.66		1.52-7.45	4.62-29.45
3	0.024-0.157		0.023-0.165	0.025-0.18	0.036-0.24

TABLE II. 95% Upper limit range across all the sky direction, on the gravitational wave energy flux ($\mathrm{erg\,cm^{-2}\,s^{-1}\,Hz^{-1}}$) from single-component and joint-index multicomponent estimations (simultaneously considering two and three spectral shapes) using the O1+O2+O3a folded dataset. Upper limit sky maps for each cases are shown in Figure 7 and 8. The increase in upper limit exhibited by the joint-index estimation is due to the increase in the variance of the corresponding estimator.

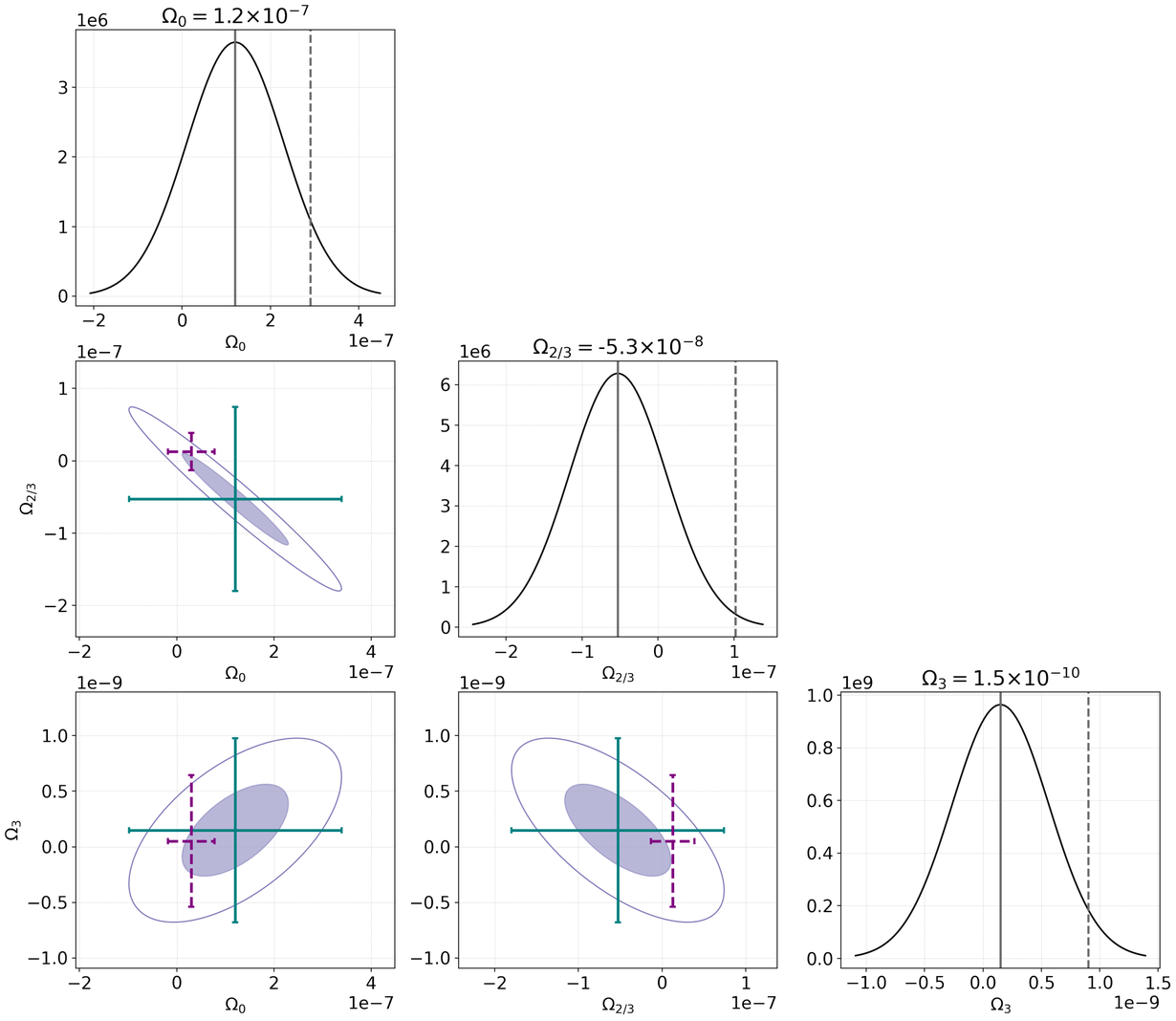

DA, J. Suresh, V. Mandic et. al. Phys. Rev. D106 043019 (2022)

Targeted Search

- Decompose source PSD

$$\mathscr{P}_p(f) = A\,\bar{H}_f\,\hat{\mathscr{P}}_p$$

Only Unknown

- MLE for scalar quantity

$$\hat{A} = \frac{\mathbf{X}^\dagger \hat{\mathscr{P}}}{\hat{\mathscr{P}}^\dagger \mathbf{\Gamma} \hat{\mathscr{P}}}$$

- Increase in SNR is expected. Immune to deconvolution problem due to forward modelling.

DA, J. Suresh, V. Mandic et. al. Phys. Rev. D106 043019 (2022)

Targeted Search for Galactic Millisecond Pulsars

$$\mathscr{P}(f,\hat{\Omega}) = \underbrace{N_{\rm obs}\langle \epsilon^2 \rangle_s}_{A}\ \underbrace{f^4\, p(f)}_{\bar{H}_f}\ \frac{32\,\pi^4\, G^2\, \langle I^2 \rangle_s}{5c^8}\, \langle r^{-2} \rangle_s\, p(\hat{\Omega})$$

Adopted PDF for Spin Frequency

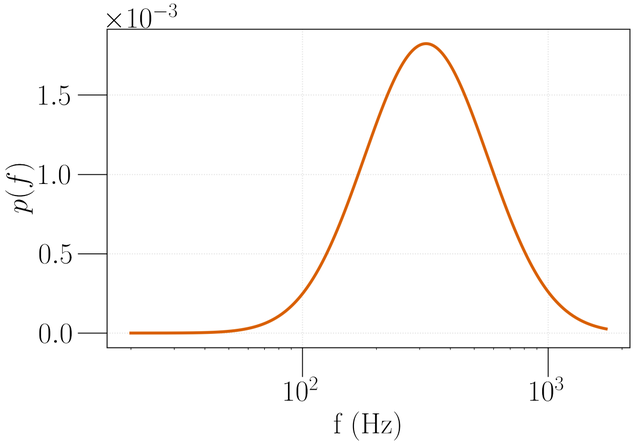

Adopted PDF for Spatial Distributions

Gaussian Radial

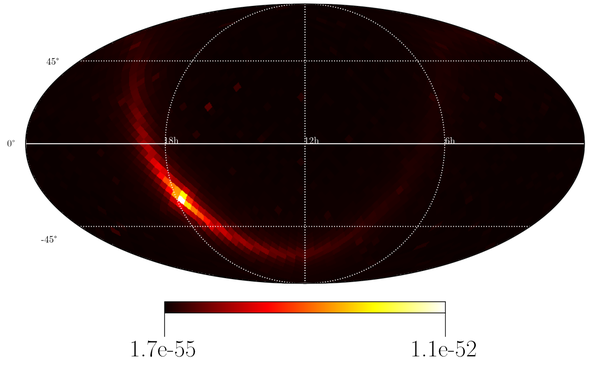

Exponential Radial

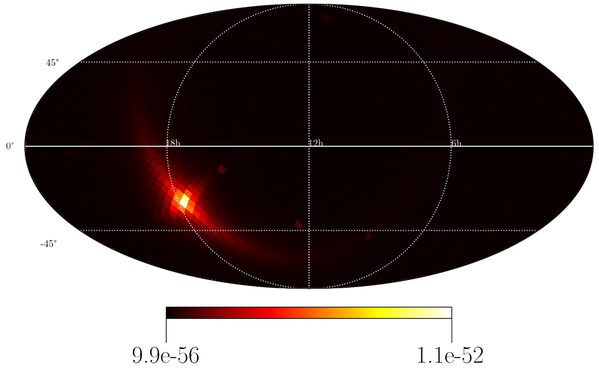

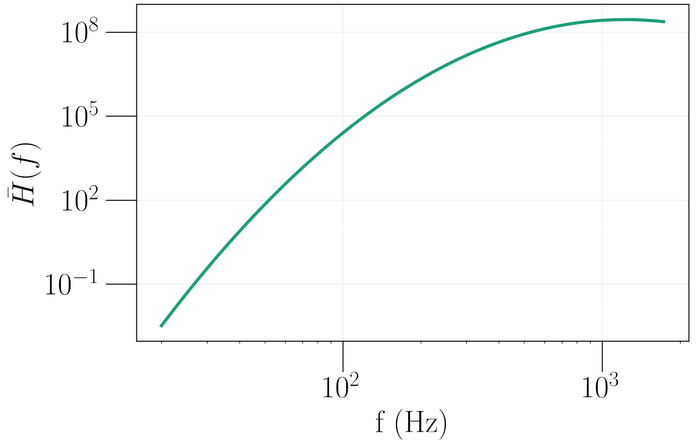

DA, J. Suresh, V. Mandic et. al. Phys. Rev. D106 043019 (2022)

Targeted Search for Galactic Millisecond Pulsars

Data Significance

O1+O2+O3 results				
Baseline	Exponential radial distribution		Gaussian radial distribution	
	$(\hat{A} \pm \sigma_{\hat{A}}) \times 10^{-8}$	$\rho_{\hat{A}}$ $(p-\text{value}\%)$	$(\hat{A} \pm \sigma_{\hat{A}}) \times 10^{-8}$	$\rho_{\hat{A}}$ $(p-\text{value}\%)$
O3-HL	5.7 ± 6.2	0.92 (18)	3.4 ± 6.3	0.54 (30)
O3-HV	120 ± 53	2.3 (1.2)	96 ± 44	2.2 (1.4)
O3-LV	17 ± 31	0.54 (29)	59 ± 29	2.0 (2.1)
O2-HL	-17 ± 24	-0.69 (76)	-8.8 ± 25	-0.36 (64)
O1-HL	-54 ± 51	-1.1 (85)	-56 ± 53	-1.1 (86)
O1+O2+O3	$\mathbf{5.4 \pm 5.8}$	**0.92 (18)**	$\mathbf{5.9 \pm 5.9}$	**1.0 (16)**

TABLE I: Here, we report the results of the targeted stochastic search analysis using the data from the first three observing runs of Advanced LIGO (H and L) and Advanced Virgo (V) detectors, hence the five individual datasets, i.e., O3-HL, O3-LV, O3-HV, O2-HL, and O1-HL and with the combined network, O1+O2+O3. The observed overall amplitude, $\hat{A}$ with the uncertainty, $\sigma_{\hat{A}}$ and SNR, $\rho_{\hat{A}}$ are obtained using the two templates for the spatial distribution created for the exponential and Gaussian distributed radial coordinate. The results are assessed through the p-value against the null hypothesis, which is that the data is pure Gaussian noise. We do not claim any detection since the obtained p-values do not pass the threshold, 5%.

DA, J. Suresh, V. Mandic et. al. Phys. Rev. D106 043019 (2022)

Targeted Search for Galactic Millisecond Pulsars

Upper Limits

- Bayesian Upper limits on the in-band numbers and averaged ellipticity.
- The best Bayesian upper limit with 95% confidence for the parameters are $N_{\rm obs} \leq 8.8 \times 10^4$ and $\mu_\epsilon \leq 1.4 \times 10^{-6}$
- Comparable to the bounds on mean ellipticity with the GW observations of the individual pulsars.

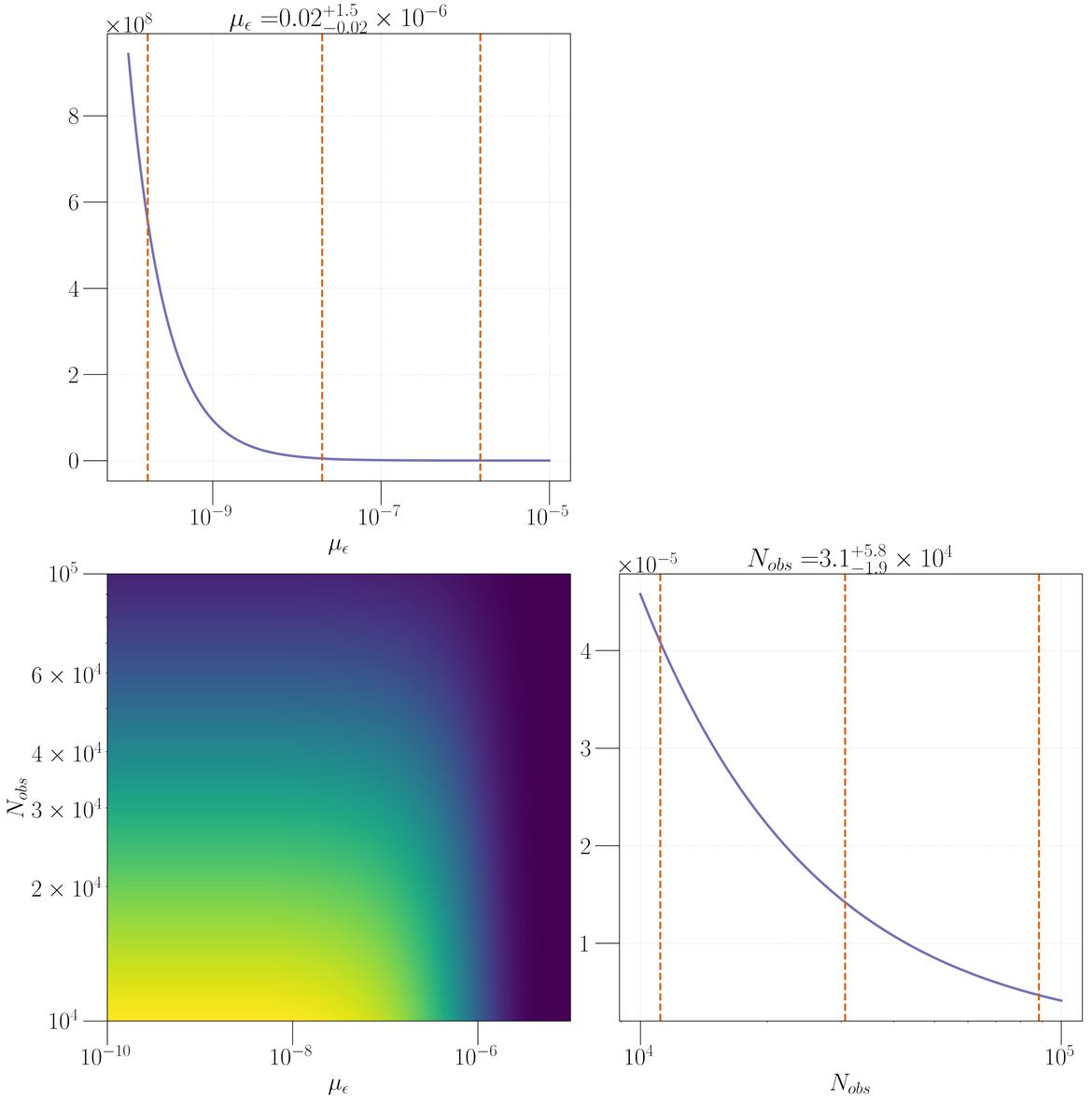

DA, J. Suresh, V. Mandic et. al. Phys. Rev. D106 043019 (2022)

Targeted Search for Galactic Millisecond Pulsars

Future Predictions

- For plausible case of $N_{\rm obs} = 4 \times 10^4$,
- One year of observations
- The one-sigma sensitivity on μ_ϵ might reach
  - 1.5×10^{-7} for the second-generation detector network having A+ sensitivity
  - 4.1×10^{-8} for third-generation detector network

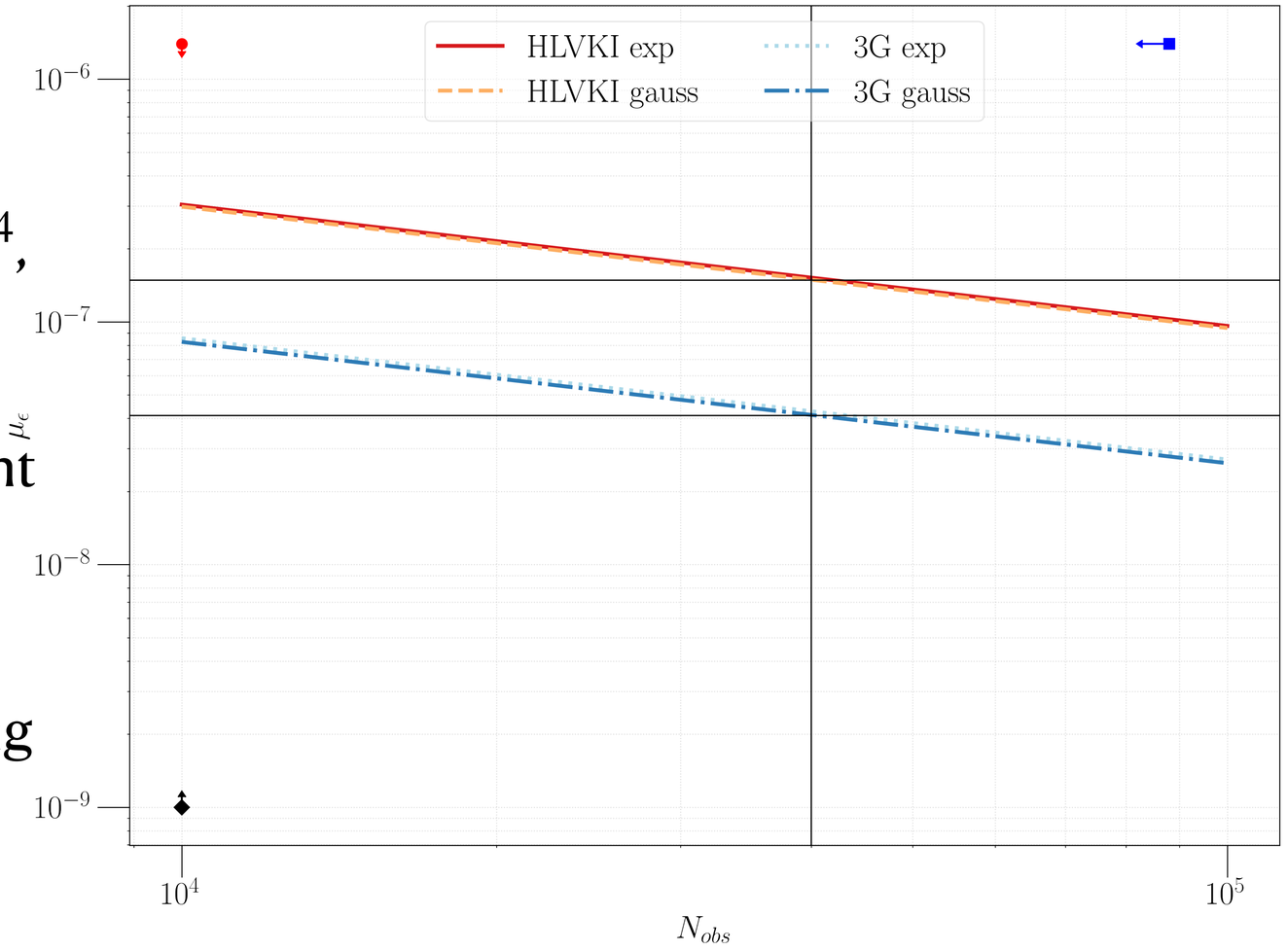

One Sigma sensitivity of future detector network in $N_{\rm obs} - \mu_\epsilon$ Plane

Conclusions

- During my PhD, I have been involved in various searches for the SGWB.

- My thesis can be broadly summarised as
  - All-sky-all-frequency searches for the point-like and extended narrowband sources of SGWB.
  - Tackling with issues involved in mapmaking for broadband SGWB.
  - Constraints on astrophysical and cosmological quantities.

Extra Slides

O2 HWI Parameters Recovery

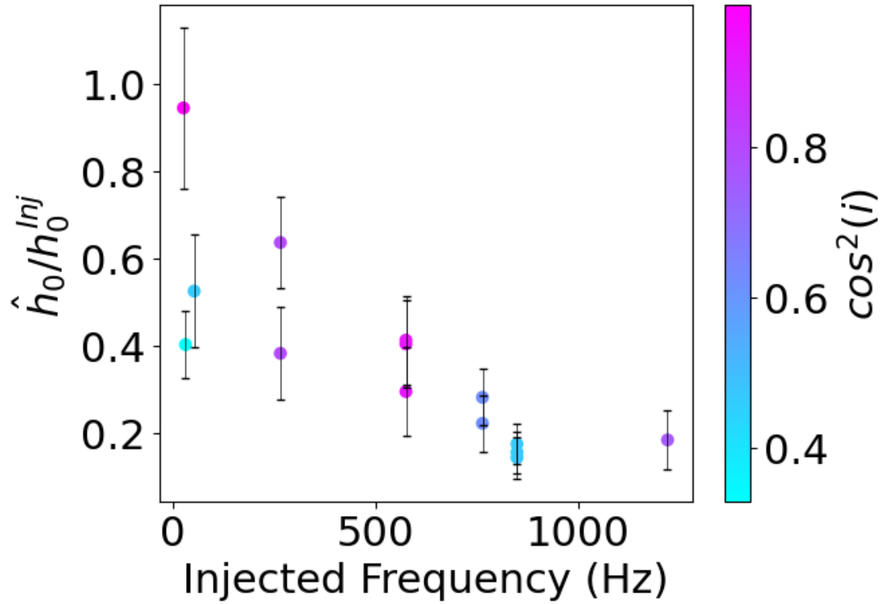

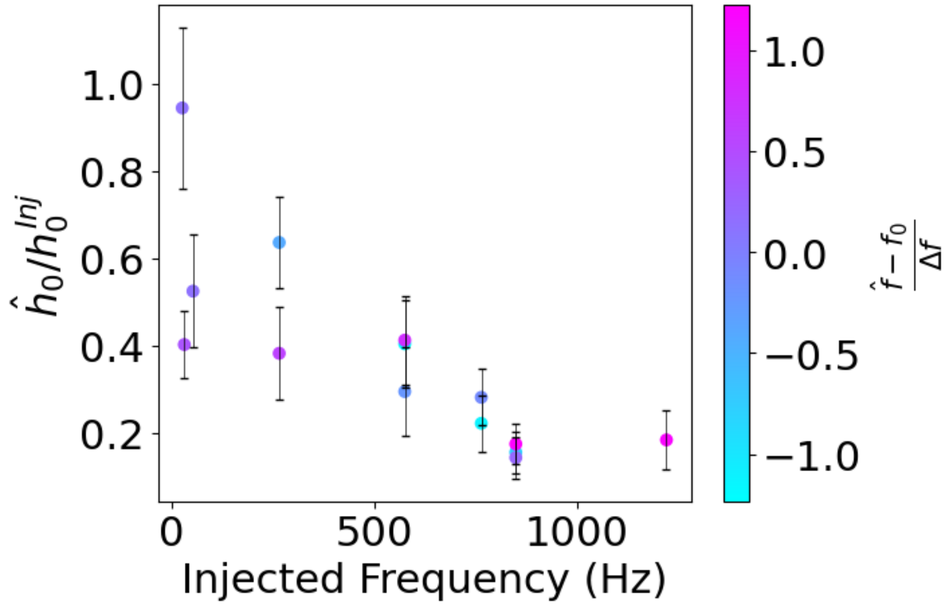

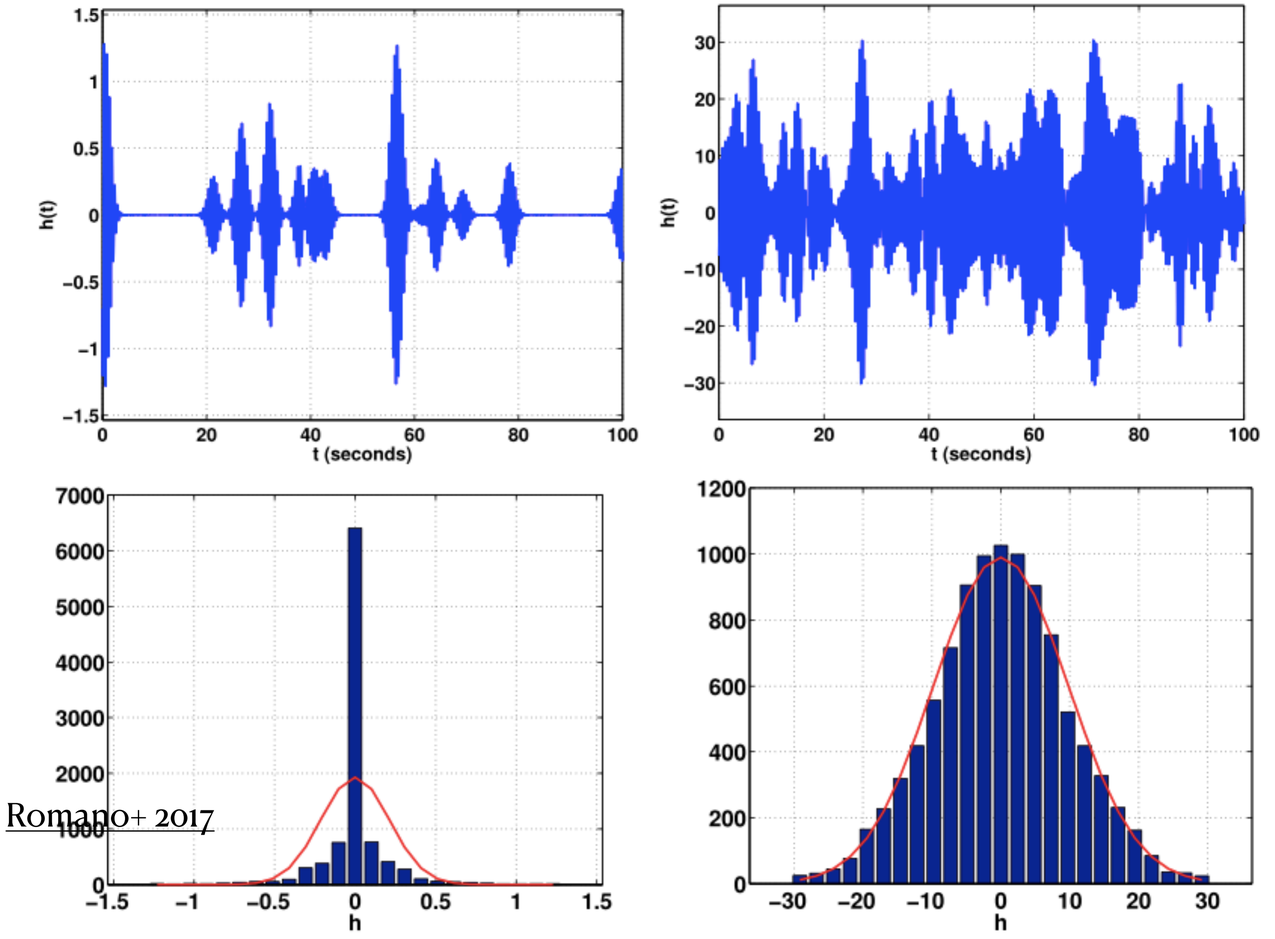

Romano+ 2017

Fig. 57 Simulated toy-model signals and histograms for different duty cycles. The *left two panels* correspond to 1 burst every 10 s (on average); the *right two panels* correspond to 100 bursts every second (on average). The *red curves* in the *bottom two panels* show the best-fit Gaussian distributions to the data. Similar to Fig. 1 from Thrane (2013)

PyStoch - Advantage

Narrowband search budget for different pipelines.

	Conventional Pipeline	Folding Pipeline	Folding & PyStoch
Intermediate Data	450 GB	1.5 GB	1.5 GB
Processing Time	10 CPU years	10 CPU days	**40 CPU minutes**
Intermediate Results	800 TB	2.5 TB	**not required**
Results	500 MB	500 MB	500 MB

Stochastic Pipeline (with folding)

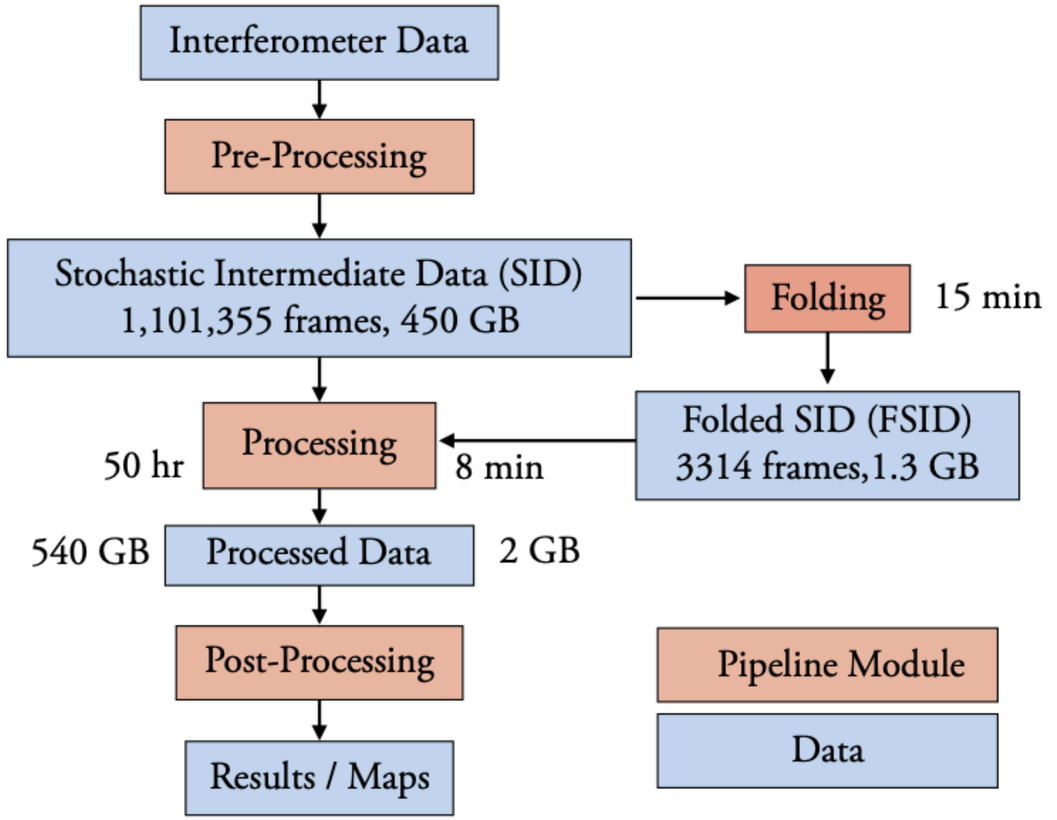

Numbers are approximate. Processing time is for 1 node in IUCAA cluster using MATLAB.